VIRTUAL WHITE MATTER:

A NOVEL SYSTEM FOR CROSS-DISH NEURAL INTERACTION AND MODULATION

A Thesis

Submitted to

the Temple University Graduate Board

In Partial Fulfillment

of the Requirements for the Degree

DOCTOR OF PHILOSOPHY

---

by

Mehdi Khantan

May 2026

Examining Committee Members:

Dr. Iyad Obeid, Advisor, Dept. of Electrical and Computer Engineering, Temple University

Dr. Joseph Picone, Dept. of Electrical and Computer Engineering, Temple University

Dr. Andrew Spence, Dept. of Bioengineering, Temple University

Dr. Mijail Demian Serruya, Raphael Center for Neurorestoration, Vickie & Jack Farber Institute for Neuroscience, Thomas Jefferson University

Dr. Alessandro Napoli, Raphael Center for Neurorestoration, Vickie & Jack Farber Institute for Neuroscience, Thomas Jefferson University

Dr. George Smith, Lewis Katz School of Medicine, Temple University

ABSTRACT

Biological Neural Networks (BNNs) are characterized by complex interregional connectivity, allowing for seamless communication between different brain regions. In vitro models traditionally consist of single-dish neural cultures that cannot reproduce the dynamics of interregional interactions. Here, we introduce Virtual White Matter (VWM), a novel platform enabling real-time functional digital connectivity between neural cultures in separate multi-electrode array (MEA) dishes. By detecting action potentials in one dish and providing precisely timed electrical stimulation to another, VWM recreates inter-regional neural communication.

VWM represents a significant advancement in *in vitro* modeling by enabling controlled interactions between heterogeneous neural cultures, such as different brain regions or cell types. The platform enables the investigation of dynamic network behaviors and integration with biological and artificial neural systems. These advances will push forward biocomputing, wetware computing, and organic intelligence. Furthermore, VWM has the potential to be applied in fields like therapeutic *interventions* that use directed neural plasticity to promote brain injury or disease responses.

This study introduces the conceptual framework, technical implementation, proof-of-concept and validation of the VWM system across two research aims. In Aim 1, the VWM platform was established by implementing precise spike detection and stimulation protocols between physically separate MEA dishes, demonstrating reliable unidirectional and bidirectional cross-dish neural communication. Machine learning classification of evoked responses confirmed that distinct, decodable activity patterns could be reliably

elicited and distinguished across dishes, with the double-threshold spike detection method successfully eliminating stimulation artifacts from the feature set.

In Aim 2, the VWM platform was extended to support structured binary communication between dissociated cortical cultures. Three-bit data words were encoded into the dissociated neural culture cell using spatiotemporal electrical stimulation patterns and decoded in real time using a Support Vector Machine (SVM) classifier trained on binned post-stimulus spike features from six selected output electrodes. A parity-based error correction scheme with confidence-based bit toggling was implemented to improve transmission fidelity. Monodirectional and bidirectional communication experiments were validated across five independent neural preparations. Longitudinal analysis demonstrated stable decoder performance across 1,600 stimulations, indicating that the stimulation protocol minimized plasticity-induced drift. These results establish that physically separated neural cultures can reliably exchange structured symbolic information through an engineered communication framework, providing a foundation for scalable, distributed biocomputing architectures. VWM is versatile, placing it at the core of a transformational tool for experimental neuroscience, biocomputing, and translational research to bridge biological and digital systems.

In Aim 1, the VWM platform was established by implementing precise spike detection and stimulation protocols between physically separate MEA dishes with a fixed 200 ms cross-dish delay. A novel double-threshold spike detection algorithm was developed and shown to be essential for eliminating stimulation artifacts from the classification feature set — when single-threshold detection was used under MK-801 silencing conditions, machine learning classifiers still achieved above-chance accuracy driven purely by artifacts,

whereas double-threshold detection correctly reduced accuracy to chance level. Machine learning classification of post-stimulus evoked responses demonstrated that distinct, decodable activity patterns could be reliably elicited and distinguished across dishes, with the first 10 ms post-stimulus window identified as the most informative period for classification. Bidirectional communication was also demonstrated, though performance was slightly lower than the unidirectional configuration due to positive feedback loop formation between the coupled cultures.

In Aim 2, three-bit binary messages were encoded via spatiotemporal electrical stimulation, decoded in real time using Support Vector Machine classification on binned post-stimulus spike features from six selected electrodes, and transmitted through a parity-based error correction scheme across five independent neural preparations. Bidirectional round-trip transmission yielded an end-to-end success rate of approximately 20%, consistent with the multiplicative error compounding across four sequential decoding stages each operating at approximately 70% word-level accuracy. The system achieved a measured information bandwidth of approximately 0.375 bits per second, constrained by inter-stimulus timing requirements imposed by post-burst recovery dynamics. Classifier performance remained stable across 1,600 stimulations in four of five preparations, confirming that the stimulation protocol did not induce significant plasticity-driven decoder degradation. Together, these results establish that physically separated biological neural networks can reliably exchange structured symbolic information through an engineered communication framework, providing a foundation for scalable distributed biocomputing architectures. Future work should address the bandwidth constraint through richer spatiotemporal encoding schemes, incorporate online adaptive classifiers to maintain decoder accuracy across extended

recording sessions, and extend the platform to organoid-based preparations and multi-node assemblies to explore emergent computation in linked biological networks.

DEDICATION

To my father — a physics teacher and bookseller — who devoted more than 45 years of his life to educating others and to me, igniting my passion for science and technology from the earliest years of my childhood.

To my mother, an elementary school teacher who spent thirty years educating children in underserved villages, and who laid the foundation of my own education with the same devotion she gave to her students.

To my sister, whose persistent encouragement has always pushed me toward greater ambition and higher achievement.

To my wife, who stood beside me at every moment of this journey, sharing the weight of every difficulty and the joy of every step forward, and who built a home and warmth around me in a country far from where we began, making every sacrifice feel like a foundation rather than a loss.

And to the neurons — biological and artificial alike — whose quiet complexity first made me ask the questions this work attempts to answer.

ACKNOWLEDGMENTS

I would like to express my deepest gratitude to my advisor, Dr. Iyad Obeid, for his guidance, intellectual generosity, and steadfast support throughout this journey. He was unfailingly professional and devoted an extraordinary amount of time to my development, not only shaping this research but also nurturing in me a more disciplined and systematic way of approaching scientific problems. His mentorship helped me build the habits of thought and inquiry that I will carry throughout my career.

I am deeply grateful to the Center for Neurorestoration at Thomas Jefferson University for providing the financial, equipment, and scientific support that sustained this work throughout its entirety. I extend particular thanks to Dr. Mijail Demian Serruya and Dr. Alessandro Napoli, whose creative ideas and innovative approaches were instrumental in shaping the direction and depth of this thesis. Their intellectual generosity and collaborative spirit enriched this work immeasurably.

I am sincerely grateful to my full committee, Dr. Joseph Picone, Dr. Andrew Spence, Dr. Mijail Demian Serruya, Dr. Alessandro Napoli, and Dr. George Smith, for their invaluable feedback, breadth of expertise, and generous investment of time. Their collective guidance strengthened this dissertation in ways both large and small.

Finally, I acknowledge the broader scientific community whose foundational contributions to neural engineering, biocomputing, and machine learning made the Virtual White Matter system conceivable. I hope this work contributes meaningfully to that ongoing and important conversation.

TABLE OF CONTENTS

TABLE OF FIGURES

1 INTRODUCTION

1.1 Background and Motivation:

Neural tissue cultures grown in multi-electrode array (MEA) dishes are widely used to study neural network development (1), learning (2), population self-organization (3), and responses to external stimuli (4). MEAs are a flexible and powerful tool for studying neural behavior because they can be used with different types of cells (e.g., with respect to species, genetic mutation, and brain region), different culture types (e.g., brain slices, dissociated cell cultures, organoids), and different morphologies (e.g., 2D, 3D). MEA cultures are an excellent platform for studying neural population function because they are simpler to interact with than in-vivo whole brains but also more biologically realistic than in silico simulations.

Closed-loop MEA systems (5) modify the open-loop MEA paradigm by enabling focal electrode stimulation in one region of the dish in response to detected activity in other regions. Such systems are emerging as prototypes of biocomputing, in which neural populations can be taught to respond differentially to different stimuli. These are effectively pattern recognition systems that use biological tissue instead of silicon-based computing. In the last three decades, there have been extensive efforts to leverage the processing capabilities of Biological Neural Networks (BNNs), including learning, adaptation, and information processing (6–12). These capabilities have been used in performing specific tasks such as controlling robots (13–15), flight control (16), and playing video games (4).

Recent examples of closed-loop MEA systems include the Dishbrain system (Cortical Labs, Melbourne, Australia), in which both human and rodent *in vitro* neural networks

exhibited learning behavior and goal-oriented activity when embodied in a simulated game world such as "Pong" (4). Another example is Brainoware (Indiana University Bloomington), which is a live brain organoid capable of learning and pattern detection in a 3D BNN (17). Brainoware has successfully predicted a Hénon map, a fundamental non-linear dynamic system characterized by chaotic dynamics. Furthermore, Sumi et al. have used BNNs as generalization filters in reservoir computing (18), a technique that enhances the performance of tasks like speech classification and pattern recognition.

Neural preparations have demonstrated potential as processing units for information, paving the way for more complex configurations of BNNs. Creating advanced forms of BNNs requires establishing connectivity between different regions or types of networks. However, the mechanisms and implications of such connectivity have not been extensively studied. The subject of this thesis, the Virtual White Matter (VWM) system, represents a pioneering effort to investigate and simulate artificial connectivity between BNNs, providing a foundation for exploring their coordinated functionality and interactions.

The VWM system extends closed-loop MEA capabilities by enabling interaction between neurons across multiple MEA dishes. As shown in Figure 1, the VWM system electrically stimulates electrodes in a target MEA dish in response to detected action potentials in a

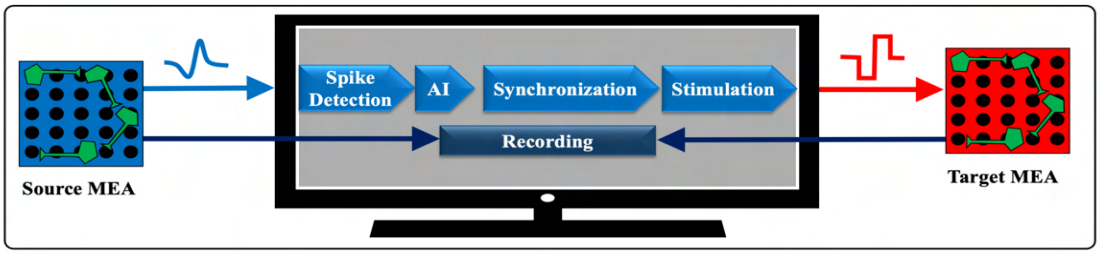

Figure 1: Schematic representative of Virtual White Matter (VWM) system.Neural signals recorded from the Source MEA undergo real-time spike detection, AI-based classification, and synchronization processing, after which a corresponding stimulation waveform is delivered to the Target MEA. A continuous recording feedback loop monitors the target network's response, enabling adaptive, bidirectional communication between two neural preparations through a central computing interface.

source MEA dish. Precision timing ensures that time- and rate-based information is preserved between the dishes. The VWM paradigm allows interaction between heterogeneous cell cultures (e.g., a dish with a hippocampal rat slice can bidirectionally communicate with a dissociated knockout mouse culture). The VWM platform can also be amended to manipulate information flow between dishes as a means of probing neural coding. For example, a target dish may only be stimulated if a certain multi-electrode pattern of activity is detected in the source. The information manipulation stage could be as simple as a pass-through follower or as sophisticated as a block of artificial intelligence, allowing for a wide range of biological computing configurations.

VWM's fundamental concept is to create a functional connection between two or more neural cultures on distinct MEA dishes in the digital world. More precisely, using VWM, one could modulate the activity of an active target neural setup in real time by providing stimulation that is contingent upon the neural activity of the source neural setup. This real-time interaction mimics the way different regions of the brain communicate with each other, allowing for the study of how changes in one region can influence another. Early closed-loop systems provided the foundation for this approach by demonstrating that recorded neural activity from one region could dynamically trigger stimulation in another, effectively providing an auxiliary interregional brain communication (19). Building on these principles, VWM not only replicates such interactions but also offers a platform for precisely controlling and manipulating the timing and pattern of information flow, enabling deeper investigations into neural coding and plasticity.

This platform has the potential to enable user-modulated communication between multiple heterogeneous cultures, which vastly expands the complexity of neural modeling. To date,

most research on BNNs has focused on single neural preparations, and little effort has been made to interconnect multiple BNNs to process information through a hybrid interconnection of the biological and digital systems. The VWM addresses this gap by enabling interconnections that could bridge multiple BNNs and ANNs, a prerequisite for biocomputing, wetware computing, and organic intelligence (17,18,20–25). Furthermore, the utilization of closed-loop stimulation systems in therapeutic environments has been investigated, with the potential to provide interventions for neurological disorders. Such applications can aid in recovery from injury or disease by directing the plasticity of the nervous system through real-time neural circuit modulation. VWM has the potential to study and replicate phenomena such as "virtual strokes," "white matter disconnection" (26,27), or “brain rewiring” (28) by selectively modulating or disrupting communication between neural populations.

Furthermore, VWM can serve as a foundational building block for implantable brain-computer interfaces (BCI), enabling reciprocal linking between spatially distant recording and stimulation elements (29). It also offers the potential to reconstruct entire mammalian brain models by interconnecting separate sections of their brain *in vivo*. This will enable the creation of more elaborate multi-specimen transfer functions or biological transformers, surpassing the capabilities of single isolated specimens. Ultimately, VWM can be a fundamental building block for virtual embodiment, in which several linked specimens could be collectively embodied in a virtual environment or in a robotic body.

This study consists of two phases. In the first phase, a proof-of-concept version of the Virtual White Matter (VWM) system has been implemented. Initially, spontaneous neural action potentials (spikes) detected in the "source" dish were used to trigger stimulations in

a "target" dish with a fixed delay of 200 ms. Subsequently, machine learning techniques classified the source of stimulation based on post-stimulus spike patterns in the "target" dish. This phase was further expanded to include bidirectional communication between the two dishes by relaying post-stimulus spikes induced in the "target" dish back to the "source" dish. The continuous feedback loop established in this manner functions autonomously, emulating interregional brain communication and providing a foundation for exploring more complex neural interactions in future research.

In the second phase, the study transitions from spontaneous neural activity to a coded message introduced into the system and subsequently identified. The message is first encoded on the first MEA and recognized via a machine learning algorithm that processes spike patterns detected in that same MEA. These spike-derived codes are then transmitted to the second MEA as stimulation signals, where they are similarly decoded by analyzing post-stimulus evoked spike patterns. This unidirectional communication setup provides a baseline for comparative analysis of encoding-decoding accuracy.

Subsequently, to evaluate bidirectional communication, the decoded message on the second MEA is re-encoded and sent back to the first MEA. Demonstrating successful decoding of this return pathway confirms the ability of the VWM system to support robust two-way communication. Finally, in a bypass step, the computer-based decoding between the two MEAs is omitted: rather than employing machine learning, the binned spike outputs from the first MEA are sent directly as stimulation signals to the second MEA, effectively using the second BNN itself as the “decoder.” This final test reveals how communication accuracy changes when the machine learning pipeline is removed, further

underscoring the potential of the VWM approach for interconnecting established BNNs and facilitating integrated neural network architectures.

1.2 Biology of Neurons

1.2.1 Structure of Neurons

Neurons, the fundamental units of the nervous system, communicate through electrical and chemical signals. Each neuron consists of three main structures: the cell body (soma), dendrites, and the axon as shown in Figure 2 (30). The soma houses the nucleus, which contains the genetic material essential for neuronal function and survival. Dendrites serve as the input zone, receiving signals from other neurons, while the axon transmits these signals to target cells. Axons vary in length, ranging from a few millimeters in the brain to several feet in the spinal cord. They may branch extensively (from 10 to 250,000 branches) to reach multiple target cells. The ends of these branches form axon terminals, where neurotransmitters are released to propagate the signal.

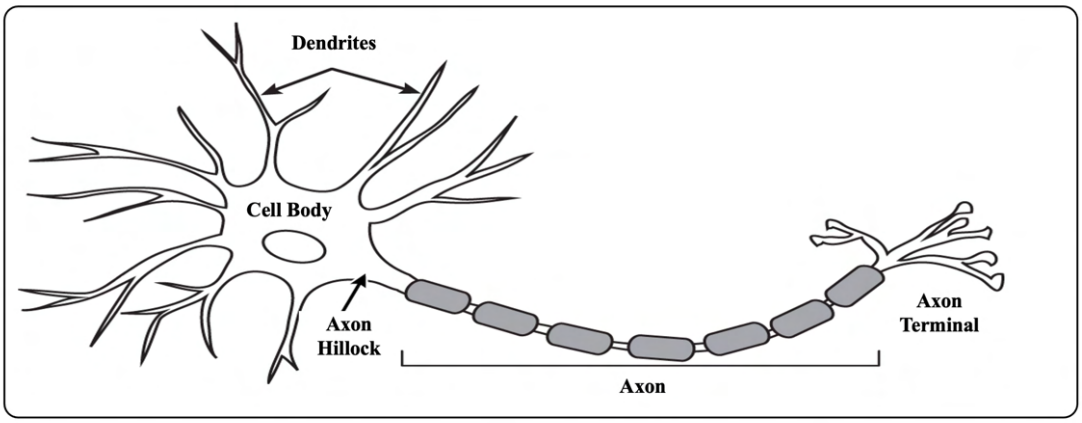

Figure 2: Schematic diagram of a myelinated neuron illustrating its principal components Including dendrites, cell body (soma), axon hillock, myelinated axon, and axon terminal. Adapted from "The Neuron" (30).

1.2.2 Neuronal Communication

The electrical properties of neurons arise from the distribution and movement of ions across the cell membrane. Key ions involved in this process include negatively charged proteins (large anions) and chloride ions (Cl^-), as well as positively charged sodium (Na^+) and potassium (K^+) ions. These ions create an electrochemical environment that determines the neuron's ability to generate and transmit signals.

Neuronal membranes contain specialized channels that regulate the ion movement. Two key types are leaky channels, which allow continuous ion flow, and voltage-gated channels, which open and close in response to voltage changes through the cell membrane. A third mechanism is provided by ion pumps, such as the sodium-potassium ATPase (Na^+/K^+-ATPase), which expend energy in the form of Adenosine Triphosphate (ATP) to actively transport Na^+ out of the cell and K^+ back in against their respective concentration gradients, maintaining the electrochemical environment necessary for signaling. Potassium (K^+) is more concentrated inside the neuron, while sodium (Na^+) is more concentrated outside. Due to the concentration gradient, potassium tends to leave the cell, but the electrical gradient pulls it back in, maintaining equilibrium. Similarly, sodium follows its own electrochemical gradient. The electrochemical equilibrium point created by these ions in tandem defines the cell's resting membrane potential.

Neuronal communication occurs through neurotransmitters, which are chemical messengers released from the presynaptic neuron. Examples include:

Dopamine: various functions, including motor control, motivation, and reward processing

Acetylcholine (ACh): commonly used by motor control neurons to communicate with muscles, facilitating movement

Endorphins: a class of neurotransmitters that play a role in pain relief, stress reduction, and the regulation of mood and immune response

These neurotransmitters bind to ligand-gated receptors on the dendrites of the postsynaptic neuron, triggering an excitatory postsynaptic potential (EPSP) or an inhibitory postsynaptic potential (IPSP) depending on the type of receptor and ion channels involved. These neurotransmitters are only released into the synaptic cleft upon the arrival of an action potential. EPSPs make the neuron more likely to fire, while IPSPs inhibit it. The axon hillock, a specialized region connecting the soma to the axon, functions as a decision-making center. If the sum of incoming EPSPs surpasses IPSPs and reaches the threshold of approximately -55 mV, an action potential is initiated. This all-or-nothing response

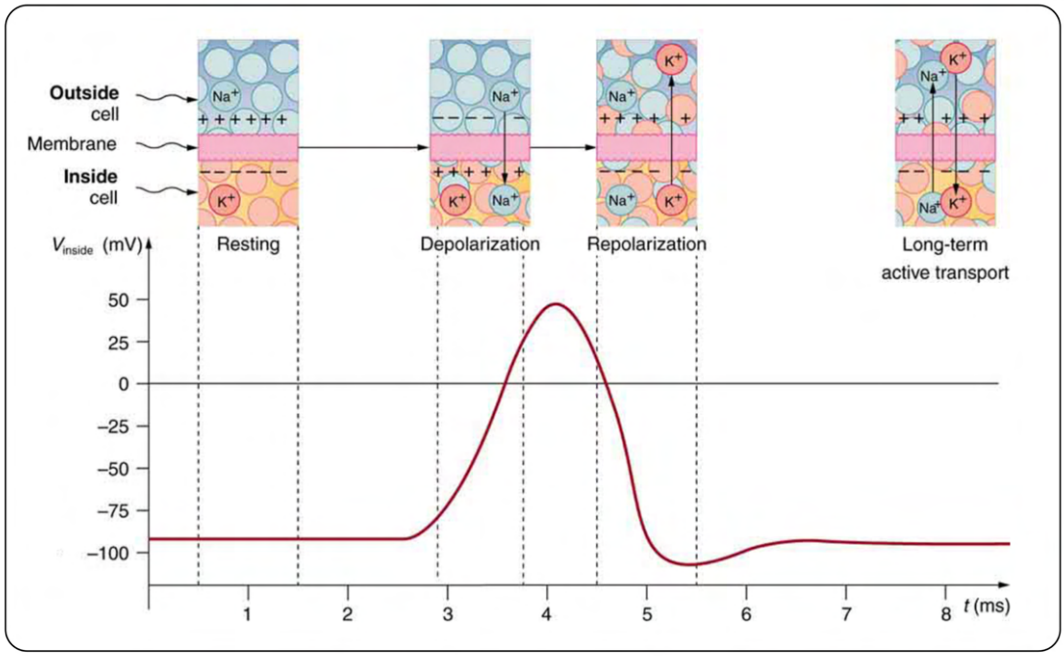

Figure 3: Ionic mechanisms underlying the neuronal action potential.The diagram illustrates the four phases of membrane potential change alongside the corresponding ion movements across the cell membrane. During the resting state, the membrane maintains a negative inside potential (aroundn−90 mV) with Na^+ concentrated extracellularly and K^+ intracellularly. Depolarization occurs as Na^+ channels open and Na^+ rushes inward, driving the membrane potential to a peak of approximately +40 mV. Repolarization follows as Na^+ channels close and K^+ efflux restores the negative potential, producing a brief hyperpolarization. Long-term active transport via the Na^+/K^+-ATPase pump re-establishes the resting ionic gradients by moving Na^+ out and K^+ back into the cell. Adapted from Nerve Conduction (31).

ensures the uniform propagation of the signal. When a neuron fires, that is essentially a spatial and temporal integration of information from upstream neurons.

An action potential propagates along the axon, and when it reaches the axon terminals, neurotransmitters are released into the synaptic cleft, continuing the cycle of neuronal communication. The stages of membrane potential changes during an action potential are shown in Figure 3 (31):

Resting Potential (about -70 mV): The neuron is at rest. The membrane voltage is maintained by sodium-potassium pumps, which exchange three Na^+ ions out of the cell for two K^+ ions into the cell (producing a net negative voltage), and by leaky channels that allow passive ion movement.

Depolarization (+30 mV): When the membrane potential reaches the threshold (~ -55 mV), voltage-gated Na^+ channels rapidly open within less than 1 millisecond, allowing Na^+ to rush into the cell. These channels have a fast activation gate that responds almost instantly to voltage changes, leading to a rapid rise in membrane voltage.

Repolarization: At peak depolarization (+30 mV), voltage-gated Na^+ channels inactivate via a built-in inactivation gate, which blocks further Na^+ influx. At the same time, voltage-gated K^+ channels begin to open, but at a slower rate (~2-5 ms delay) compared to Na^+ channels. This delayed opening allows K^+ to exit the cell, restoring a negative membrane potential.

Hyperpolarization (< -70 mV): Because K^+ channels close more slowly than Na^+ channels, delayed rectifier K^+ channels remain open for a short period after repolarization, causing the membrane potential to temporarily become more negative than resting levels.

Restoration: Once K^+ channels finally close, the sodium-potassium pump actively restores ion balance by pumping Na^+ out and K^+ back into the cell, bringing the membrane potential back to its resting state.

These molecular mechanisms highlight how the specific biophysics of membrane proteins shape neuronal electrical activity and how even minor alterations, such as genetics affecting ion channel functions, can lead to profound physiological consequences. These include epilepsy, certain migraines, and long QT syndrome as well as neuromuscular disorders, chronic pain conditions, neurodevelopmental diseases, and neurodegenerative disorders (32–34).

1.3 Microelectrode Arrays

1.3.1 How Microelectrode Arrays Work

Microelectrode arrays (MEAs) integrate electrodes into *in vitro* neural cell cultures to detect their extracellular electrical signals and to deliver targeted electrical stimulation. The functionality of MEAs is based on the electrophysiological properties of excitable neurons. Neurons generate ionic currents across their membranes, leading to extracellular voltage fluctuations that MEAs can detect. During recording, these electrodes sense voltage changes in the extracellular medium and convert them into electronic signals. During stimulation, they deliver electrical pulses, which generate ionic currents in the surrounding medium that modulate neural activity. The quality of recordings depends on multiple factors, including electrode geometry, impedance, and the quality of cell-electrode coupling.

When an electrode is placed in an ionic solution (such as a neural culture medium or cerebrospinal fluid), an electrical double layer forms at the interface due to charge

redistribution. This interface behaves as a capacitor but also exhibits resistive properties, which influence signal quality and impedance. The first layer, which is the electrode surface, carries free-moving electrons, as it is a metal. The second layer is the electrolyte side, in which ions in the surrounding solution rearrange in response to the electrode's charge. These two layers of opposite charges act just like the two plates of a capacitor, one plate being the electrode's surface and the other being the charged ions in solution (35).

MEA recordings capture either action potentials representing activity from a single neuron or local field potentials (LFPs), which are low frequency fluctuations representing activity from multiple neurons. While all extracellularly recorded action potentials share a similar shape (a negative version of the neuron's membrane voltage that was shown on Figure 3) their amplitude varies based on neuron size, axon properties, ion channel composition, media conductivity, and the distance between the neuron and the electrode. Larger neurons with thicker axons generate higher voltage in vicinity of their membrane, and this voltage attenuates approximately with the inverse of distance from the membrane of the cell (36). Depending on electrode size and neuronal density, a single electrode can record signals from multiple nearby neurons, resulting in overlapping extracellular voltages. Researchers use mathematical techniques such as spike sorting to separate these signals, though this process can be computationally demanding (37,38). To ease the signal isolation process, high-density MEAs with smaller and less electrode pitch (center-to-center distance between the conductive areas of two electrodes) have been developed, positioning each electrode closer to individual neurons and covering all essential neuronal space. These designs enhance spatial resolution by reducing the number of neurons contributing to each electrode's signal. However, decreasing the size of the electrodes increases their impedance

which in turn makes the captured signal weaker and more susceptible to noise. Addressing these challenges requires amplifiers with higher input impedance (on the order of hundreds of megaohms) and the adding some software techniques for signal processing to remove the unwanted noise. A new method for spike detection has been devised and is discussed in detail in Section 2.4 Realtime Spike Detection.

1.3.2 Materials and Fabrication:

Microelectrode arrays are built from biocompatible conductive materials and insulating substrates that together determine their performance and longevity. Noble metals like platinum (Pt) and gold (Au) are commonly used because they resist corrosion and are biologically inert (39). Platinum-iridium alloys (Pt-Ir) and iridium (often as iridium oxide, IrO2) are also widely used for their high strength and high charge-injection capacity (40). In contrast, materials like copper or silver are avoided despite excellent conductivity, since they corrode or leach toxins in tissue (39). To improve signal quality, electrode surfaces are often coated to lower impedance: for example, depositing platinum black, iridium oxide, or titanium nitride (TiN) can reduce a 50 μm electrode's impedance to ~10–20 kΩ at 1 kHz

1.3.3 In-Vitro Microelectrode Arrays

Planar MEAs used for *in vitro* research are typically transparent MEAs with a grid of microelectrodes embedded in a dish or slide, allowing neurons or cardiac cells to grow over the electrodes. A common configuration is a 6×10 or 8×8 electrode grid (60–64 electrodes total) covering a few square millimeters. For example, the MED64 (Alpha MED Scientific, Osaka, Japan) probe (Figure 4A) has 64 electrodes with electrode sizes of 20 μm or 50 μm and arranged with center-to-center spacings of 100–450 μm (41). These electrodes are

typically flat pads made of noble metal or conductive ceramic. Indium tin oxide (ITO) film is often used for the underlying tracks due to its transparency, and the electrode sites are coated with a low-impedance material like platinum black or TiN. TiN-coated electrodes 30 μm in diameter have impedance on the order of 100 kΩ at 1 kHz, while 50 μm Pt-black electrodes can be 20 kΩ, yielding an excellent signal-to-noise ratio for extracellular spikes. Planar MEAs often include large reference electrodes (typically in the 4 corners of the array) and can support stimulation on any site. These dish-based MEAs allow long-term recordings from cultured networks or acute brain slices and can be reused a multiple times with proper care (41). More recently, high-density CMOS MEAs have greatly expanded *in vitro* capabilities. In these devices, each electrode is integrated with on-chip amplifiers and multiplexers, enabling thousands of electrodes to be recorded simultaneously. A prime example is 3Brain's (Pfäffikon SZ, Switzerland) BioCAM DupleX, which features a 4,096-electrode array on a 2.7×2.7 mm silicon chip, arranged as a 64×64 grid. Each electrode on this CMOS-MEA is 21 μm square with a 42 μm pitch, and all 4,096 channels can be sampled simultaneously at 20 kHz (42). This technology achieves sub-cellular resolution, essentially "imaging" electrical activity without a microscope. The BioCAM DupleX system (43) records from 4096 electrodes in parallel, capturing both single-neuron spikes and local field potentials propagation across brain slices. Materials for CMOS MEAs must be fully integrated – 3Brain uses platinum-coated electrodes on CMOS to ensure biocompatibility and low noise (see Figure 4G).

1.3.4 In vivo and Implantable Microelectrode Arrays

In vivo MEAs are specially designed for implantation, either sitting on the surface of neural tissue or penetrating it to record extracellular activity. They are generally categorized by

form-factor: microwire arrays, silicon microfabricated arrays (e.g. Michigan and Utah probes), and flexible polymer arrays. These devices differ in electrode density, geometry, and tissue response.

Microwire MEAs consist of fine wires (typically 30–50 μm diameter) inserted into the brain, often bundled in arrays of 4 to 64 or more. The wires are insulated (with polyimide, parylene, glass, or Teflon) except at the tip, which serves as the recording site (39). Common materials are tungsten, stainless steel, or Pt/Ir wires, chosen for stiffness to penetrate brain tissue yet resilience against bending. Each wire records spiking activity from neurons in a small 50–100 μm radius volume around its tip. Variants like tetrodes (four twisted microwires) improve single-unit isolation by recording each neuron on multiple closely spaced tips.

Silicon-based MEAs are fabricated by MEMS processes, yielding more complex geometries and higher site counts on rigid shanks. There are two classic designs, named for the universities where they were developed. Michigan Arrays are planar polysilicon or silicon probes with multiple recording sites distributed along the length of a thin shank. Each Michigan probe is typically 15 μm thick and 50 μm wide, with a sharp tip, and several electrode contacts (pads of 10–20 μm) arranged in different forms from tip to base as shown in Figure 4B (44). Probes can also have multiple shanks: e.g. a 4-shank device with eight electrodes per shank yields 32 channels in one implant (39). The rigid silicon substrate minimizes bending during insertion, giving precise electrode placement. Their advantage is the ability to capture laminar activity profiles – recording neurons at different depths (multisite vertical recordings to study cortical columnar activity, etc. However, the flat shank can cause more tissue damage and displacement than thin wire, and the high

channel count can introduce crosstalk due to inter-track capacitance (39). Modern versions include on-shank electronics: the Neuropixels (Leuven, Belgium) probe is essentially a

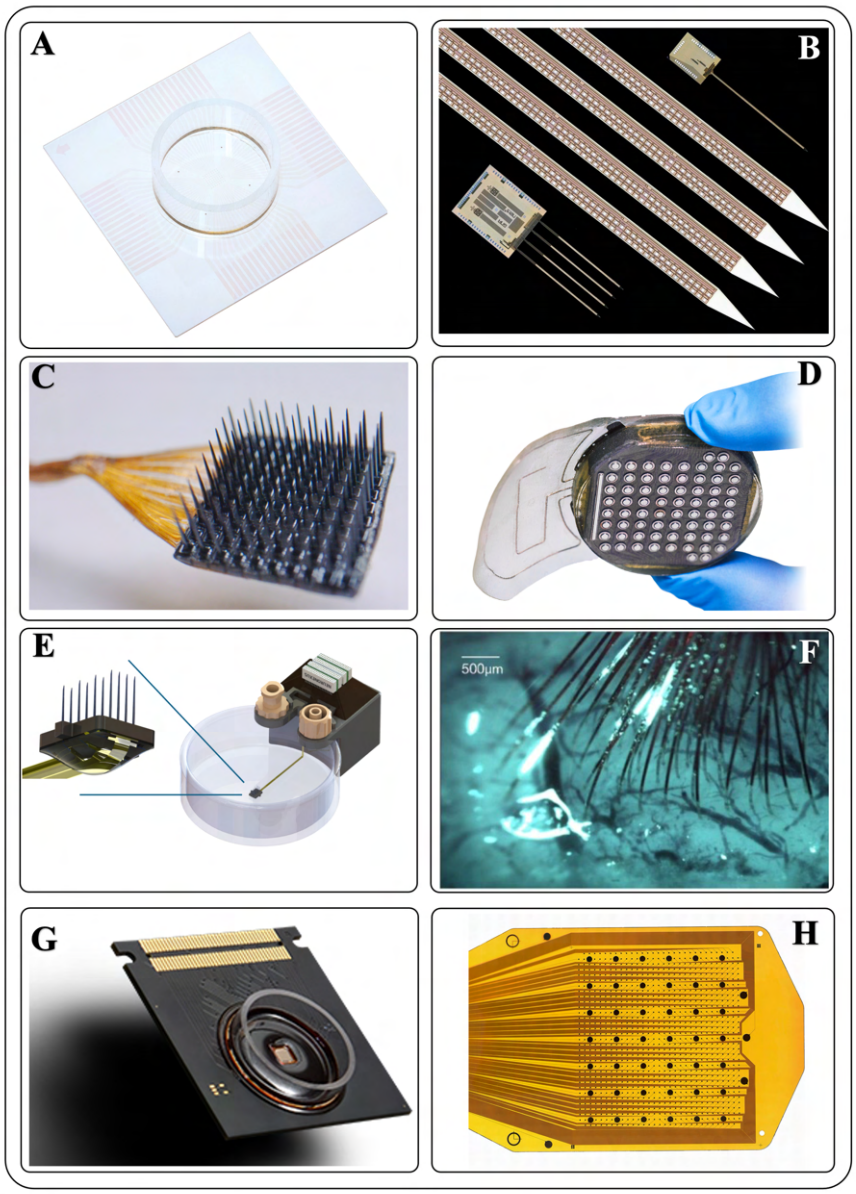

Figure 4 Representative examples of Micro Electrode Array (MEA) technologies across different application scales. (A) MED-64 planar MEA for in vitro and ex vivo applications Adapted from MED6 (41). (B) Neuronexus Michigan Arrays used in in vivo animal studies. Adapted from Neuronexus (44) (C) Blackrock Neurotech Utah Array for human intracortical recording. Adapted from BlackRock (40). (D) WIMAGINE ECoG Array for human cortical surface recording. Adapted from WIMAGINE (57). (E) Proposed MEA system for ex vivo studies, showing electrode interface and recording chamber. (F) Neuralink flexible electrodes implanted in a rat brain. Adapted from Neuralink (59). (G) 3Brain high-density CMOS-based MEA featuring integrated on-chip amplification and multiplexing for high-resolution in vitro neural activity mapping. Adapted from 3brain (43). (H) Precision Neuroscience Layer 7 cortical electrode array, a high-density flexible ECoG device designed for minimally invasive deployment on the human cortical surface. Adapted from Precision (58).

CMOS-Michigan hybrid, with 960 recording sites on a 10 mm length shank, 70 μm wide (45). In Neuropixels, 384 sites can be selected to record at once (out of 960), and integrated amplifiers allow this enormous scale without overwhelming noise. This represents an order-of-magnitude leap in channel count, enabling brain-wide recordings with single-cell resolution in rodents. Michigan arrays have evolved from early 16-channel probes to state-of-the-art 1000-channel microsystems, all leveraging silicon microfabrication for precision and density.

In contrast to the thin planar Michigan style, the Utah array is a 3D bed-of-nails configuration. It consists of a grid of silicon needles (typically 100 needles in a 10×10 array over a 4 mm×4 mm area) etched from a single silicon block. Each needle is around 80μm radius at the base and tapers to a sharp tip (around 1μm tip radius), with single metal electrode site located at the tip. All needles are the same height (commonly 1.0 or 1.5 mm for cortex) so that the array records from approximately one cortical layer (a horizontal array of sites at uniform depth). The electrodes are connected via metallization through the base to a connector (e.g. a ceramic CerePort, BlackRock Neurotech, Utah, USA) (46). The standard Utah array, commercialized by Blackrock Microsystems, has 96 active electrodes (4 corner needles are often inactive for mounting) and is FDA-approved for human research which is shown in Figure 4C (40). Key specifications include a 400μm inter-electrode pitch , needle length options from 0.5 mm up to 1.5 mm, and tip metallization with platinum or iridium oxide. The Utah array's design enables recording from hundreds of neurons simultaneously, since each microelectrode can pick up multiple units in its vicinity and the array spans a broad surface area (e.g. 4 × 4 mm of cortex). It has been used in many brain-machine interface demonstrations; for example implanted Utah arrays in motor cortex have

allowed humans to control robotic arms (47–49) or detect handwriting (50,51,51).. The array is also used in neuroscience for recording population activity and in neuro prosthetics for stimulation (each needle can deliver localized microstimulation) (52). Utah arrays are considered the “gold standard” for multi-unit cortical recordings, with over two decades of use and over 20,000 citations in the literature (39).

In general, the Michigan and Utah arrays are regarded as state-of-the-art penetrating MEAs and represent two paradigms. The Michigan array provides precise vertical sampling with multiple electrodes per shank, whereas the Utah array maximizes horizontal coverage with a single electrode per shank and numerous shanks. The Utah arrays, which are commercialized by Blackrock Microsystems, have been approved by the FDA for human implantation and are now used in clinical research settings. In contrast, the Michigan arrays have not been approved for human clinical use and are primarily used in animal studies (39,53).

Flexible Arrays replace rigid silicon or metal based MEAs with polymer materials (e.g. polyimide, Parylene, SU-8) that better match the brain’s stiffness. The motivation is to minimize chronic tissue reaction caused by micromotion of a stiff implant against softer neural tissue. Flexible arrays can bend and move with the brain, causing less strain and inflammation over time The stiffness of the materials is being measured by Young's modulus (E) which is a property of the material that tells us how easily it can stretch and deform and is defined as the ratio of tensile stress (σ) to tensile strain (ε). Stress is the amount of force applied per unit area ($\sigma = F/A$) and strain is extension per unit length ($\varepsilon =$ dl/l). Young’s modulus of polyimide is around 2.5 GPa vs silicon’s is around 200 GPa, which shows their difference in terms of stiffness, while the brain tissue is much softer (E

= 0.4–15 kPa) (54). The mismatch between the stiffness of the brain tissue and the implanted microelectrode can lead to low and long-term inflammation due to micromovements of the brain tissue (39,55,56). Typical examples include thin-film polyimide probes with metal traces (often gold or platinum) with multiple electrodes on each shank similar to Michigan probes, but only 5–20 μm thick and with significantly reduced stiffness.

Another category is surface-conforming arrays, such as electrocorticography (ECoG) grids, which are made of silicone or polyimide with embedded electrodes placed on the brain surface. However, these arrays record local field potentials rather than individual spikes. ECoG is a neural recording technique that uses surface electrodes positioned directly on the cortical surface to measure electrical activity. ECoG arrays are commonly used in clinical settings for pre-surgical epilepsy mapping and have recently gained attention in research on brain-computer interfaces (BCIs) (57). A sample of these MEAs is shown in Figure 4D (57). ECoG arrays are classified as subdural electrodes, meaning they sit on the exposed brain surface without penetrating tissue. The electrode contacts are typically made of platinum-iridium (Pt-Ir) or gold (Au) and are embedded in a flexible, biocompatible polymer substrate such as silicone, polyimide, or Parylene-C.

A recent advancement in this category is the Precision Neuroscience Layer 7 Cortical Interface, shown in Figure 4H (58), which features a high-density flexible polyimide array with hundreds of electrode sites designed for minimally invasive deployment onto the human cortical surface through a small cranial incision, enabling broad spatial coverage with reduced surgical risk.

Another notable design is Neuralink's thread-like electrodes (59): ultra-fine polyimide filaments (around 5–6 μm width) with embedded gold traces and 32–64 recording sites along each filament as shown in Figure 4F (59). The stiffness of the threads are so low that they cannot be inserted by themselves so Neuralink developed a micro-surgical robot (60) to insert them reliably into cortex. Once implanted, their flexibility virtually eliminates large micromotion forces, greatly reducing vascular damage (the robot can avoid blood vessels with micron precision) and inflammatory responses.

1.3.5 Custom Ex Vivo Microelectrode Arrays

In addition to conventional *in vitro* and *in vivo* MEAs, we developed and evaluated a new generation of 3D *ex vivo* MEA systems for recording and stimulating neural tissue preparations, including brain slices (see Figure 4E). While these 3D MEAs were not used in the present study, they will be implemented in future VWM development. We acquired Neuronexus Michigan Array Shanks (Model 4x8-prox-2mm-150-400-177, Neuronexus, Ann Arbor, MI, USA) and positioned them upright to allow brain slices to be placed and gently penetrated onto the shanks. Additionally, we designed a custom dish holder with an integrated automatic media exchange system, enabling continuous media change. This setup facilitates simultaneous neural recording and stimulation while optimizing conditions for long-term activity monitoring.

2 SYSTEM CONFIGURATION

2.1 Cell Preparation

To conduct Aims 1 and 2, dissociated cortical neurons were cultured directly on MED64 P515A MEAs (Alpha MED Scientific, Osaka, Japan) for 14 to 50 days. The MED64 system is a commercial 2D *in vitro* MEA platform featuring 64 planar platinum microelectrodes arranged in an 8×8 grid on a glass plate, each 50×50 μm² in size and spaced 150 μm apart, housed in a 10 mm-high package that enables measurement of neuronal activity in dissociated cells, organotypic slice cultures, and tissue slices. The platinum electrodes are coated with platinum black to lower impedance and improve signal quality.

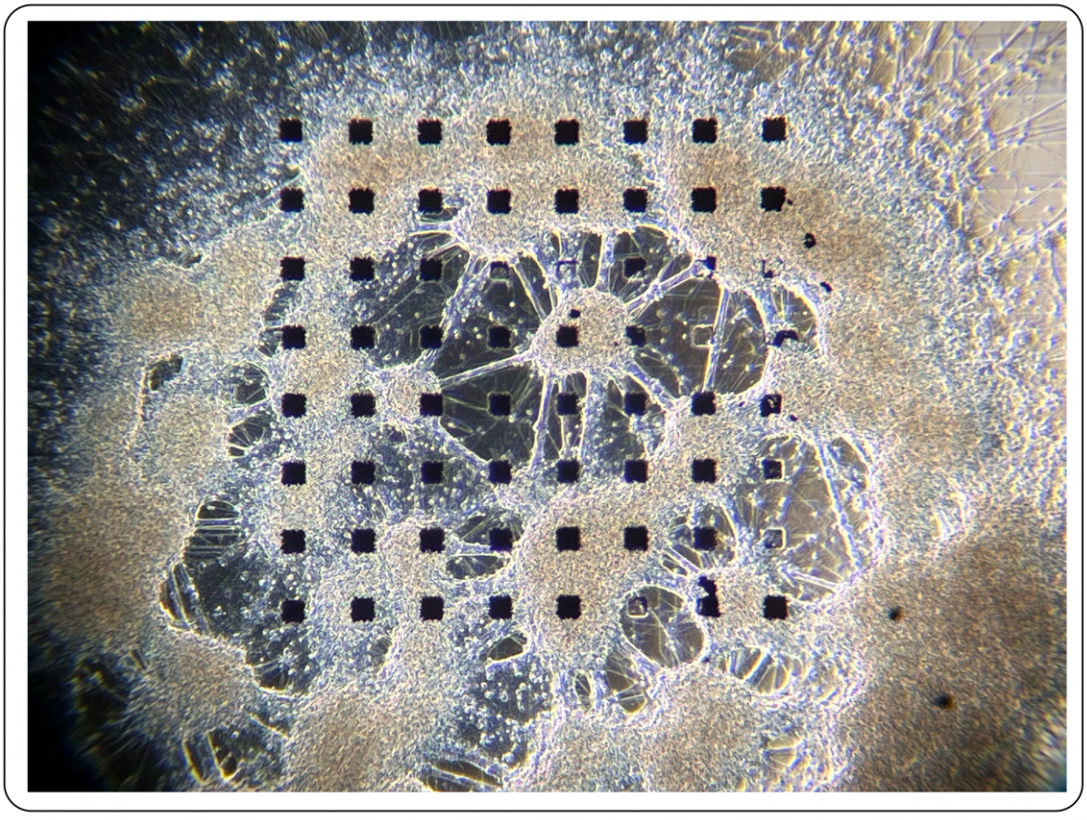

Figure 5: Brightfield microscopic image of neural cells cultured on a planar MEA. The square-shaped recording electrodes arranged in a grid pattern are visible beneath a confluent network of neurons and glial cells. Neuronal soma and extending neurite processes span across multiple electrode sites, demonstrating successful cell adhesion and network formation on the MEA substrate.

Cortical neurons were isolated from embryonic day 18 (E18) rat cortices under a protocol approved by the Institutional Animal Care and Use Committee (IACUC). Prior to cell placement, the MEAs were coated with a 20 µg/ml solution of poly-D-lysine (PDL) to enhance cell adhesion. After a 30-minute incubation, the PDL solution was removed and the MEAs were rinsed three times with sterile water to eliminate any excess. A 2 µg/ml laminin solution was then applied, incubated for 30 minutes, removed, and followed by three additional rinses with sterile water. Approximately 50,000 cortical neurons were plated onto each MEA and maintained in an incubator at 37°C with 5% CO_2 in Neurobasal-A medium supplemented with B-27 and GlutaMAX (NB Active 4 media). The culture medium was refreshed by replacing approximately 60% of the volume twice per week. Neural activity typically began to manifest around day 14 post-plating and was sustained until approximately day 48. Figure 5 shows a microscopic image of the cells on the MEA at 30 days post-plating.

2.2 Data Acquisition and Electrical Stimulation System

A top-level system block diagram is shown in Figure 6. Each MEA contains 64 electrodes, and the system simultaneously interfaced with two MEAs. Each MEA was placed in an MEA connector (MED-C03, Alpha MED Scientific) and connected to the recording and stimulation system via a custom adapter. The adaptor PCBs were custom designed using Altium Designer software and hand soldered after printing. These custom adapters bridged the MEA connectors to two 32-channel Intan (Los Angeles, CA) M4032 RHS stim/record headstages to create a 64-channel bidirectional link for each MEA (See Figure 7). Each

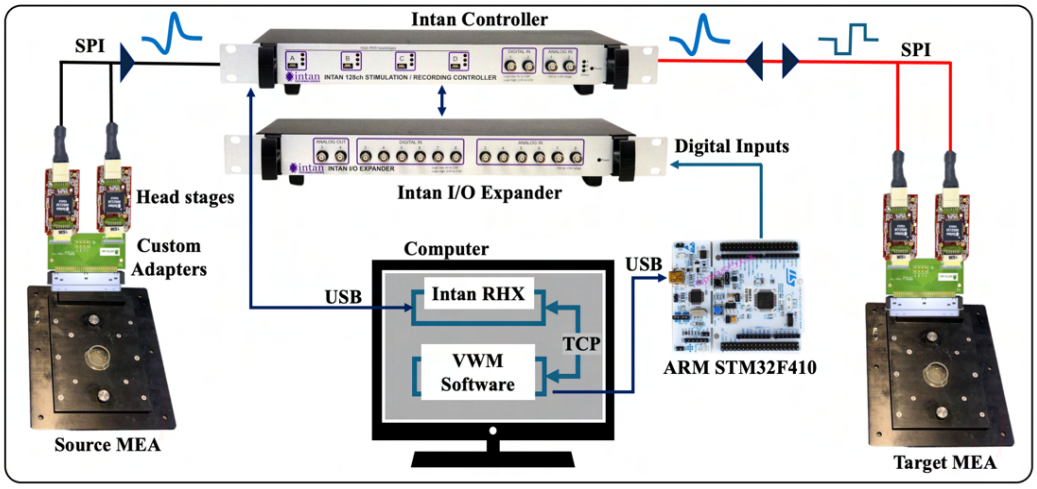

Figure 6 Block Diagram of Virtual White Matter (VWM) at System level.

M4032 headstage contains two Intan RHS2116 16-channel stim/amplifier chips, together providing 32 bidirectional channels per headstage. Intan headstages are high-density miniature PCBs positioned in close proximity to the electrodes that amplify and digitize neural signals, ensuring that all data transmitted through the interface cables is purely digital and immune to noise, supporting data recording at sampling rates of up to 30 kSamples/s and current-controlled electrode stimulation.

Since the system interfaced with two MEAs, a total of four 32-channel headstages were employed, fully utilizing the 128-channel capacity of the Intan system. A bidirectional link connected the headstages to a 128-channel controller unit (RHS, Intan), which in turn relayed data and control to a personal computer via USB. The acquisition computer used a conventional multithreaded architecture to run in parallel the stock Intan software I/O package (RHX) for acquisition system management and data acquisition and a custom VWM Software for real-time data processing and stimulation control. These parallel application threads communicated via a local TCP socket. Once the VWM software detected a spike in the source dish that met certain criteria, a stimulation command was

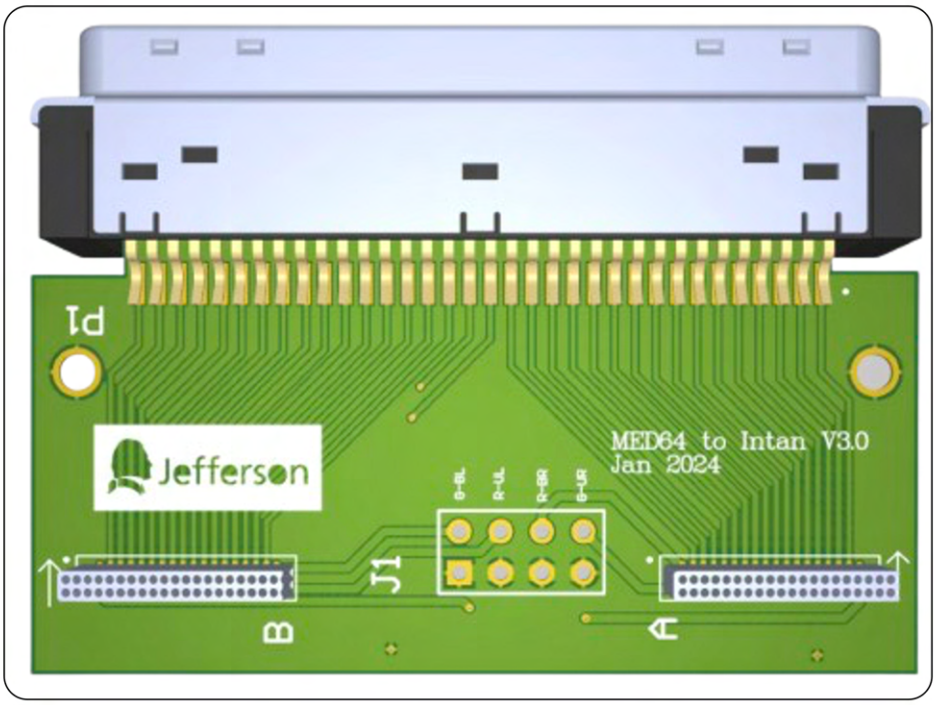

Figure 7 Custom designed adaptors for bridging the MEA connectors to two 32-channel Intan M4032 RHS stim/record headstages.

passed to an ARM microprocessor (STM32F410, STMicroelectronics, Plan-les-Ouates, Switzerland), which synchronized and buffered stimuli across channels before triggering the controller to stimulate the target MEA. An I/O expander (E6500, Intan) provided supplemental digital I/Os, enabling seamless relay of stimulation commands from the microcontroller to the Intan controller.

To deliver stimulation patterns to the Intan head stages, two primary methods can be employed. The first is to send stimulation commands through the TCP Command Port. Testing revealed that the delays associated with this method due to transmission through the TCP Command Port, Intan RHX software, and the universal serial bus (USB) were inconsistent, a critical limitation arising from the non-deterministic timing behavior of the operating system, which cannot guarantee precise or repeatable command execution times. To achieve consistent delays, a second method was developed in which stimuli were

digitally triggered through the I/Os of the Intan expansion box. This method required the use of an STM32F407 microcontroller, receiving stimulation commands through USB, with an onboard circular buffer implemented to compensate for any timing inconsistencies in data recording or software-based signal processing. The circular buffer allowed asynchronous data input and synchronous output, ensuring precise timing.

Prior to stimulation, the VWM software preprograms the stimulation parameters, including pulse shape, amplitude, pulse width, number of pulses, etc. into the Intan controller. The stimulation trigger of each target electrode is assigned to a digital input signal on the Intan expansion box. The microcontroller generates these triggering pulses based on the commands received from the VWM software via USB in real time. Each rising edge of a pulse on the expansion box's digital input activated the preprogrammed stimulation on the

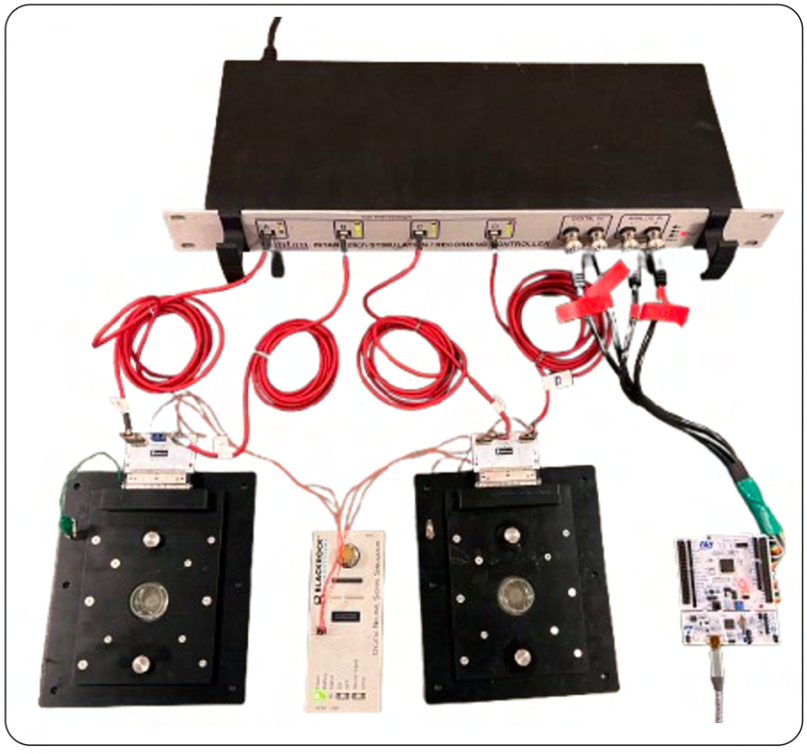

Figure 8 Experimental setup for testing signal processing and spike detection using Blackrock neurostimulator.

corresponding electrode, with the expansion box relaying the stimulation triggers to the Intan controller. This entire synchronization process occurred within the firmware of the microcontroller and the Intan system, avoiding variability associated with operating systems and ensuring consistent timing. The final stimulation commands were transmitted to the headstages via Serial Peripheral Interface (SPI) cables.

To minimize stimulation-induced artifacts and amplifier railing—which occurs when stimulation voltages exceed the system's maximum readable voltage (6.4 mV for the Intan RHS system)—some neural recording devices offer blanking hardware features, namely the capability to completely turn off the amplifier and zero out the recording for a predefined time both pre- and post-stimulus to reduce artifacts caused by stimulation. However, this approach could potentially destabilize IIR filters due to DC-offset issues during the initiation phase following the zero-out period. Since this feature is not available in the Intan system, an alternative method was employed to address these artifacts. The Intan system was configured to temporarily reduce the amplification gain across all electrodes of the stimulated head stage during the stimulation. While a low-pass filter (with Intan's default setting at 1000 Hz) is commonly used to filter out these high-frequency artifacts, it proved impractical because the initiation of the filter prior to stimulation introduced start-up artifacts, especially in the presence of residual DC voltage from previous stimulations. By instead reducing the amplification during stimulation, these issues were mitigated, leading to more accurate signal detection and reduced artifact impact (61).

Before working with actual neurons on the MEA, we developed a minimal bench simulation system, as shown in Figure 8. This system utilized a Blackrock Digital Neural

Signal Simulator (PN-8282, Blackrock Microsystems, LLC, Salt Lake City, UT) to generate simulated neural activity. The simulator produced a baseline of low-frequency activity along with various modes of high-frequency spikes, including phases of normal single spikes and bursts. The outputs from the Digital Neural Signal Simulator were connected to the MEA inputs, simulating neural activity within the dish. This setup allowed us to develop and refine the system efficiently, minimizing the time spent on cell culturing and experimental preparation.

2.3 VWM Software

Figure 9 shows a detailed block diagram of the custom VWM software package and its interaction with the external hardware components. The software was written in standard Python 3.0 for ease of implementation and portability between operating systems. The code is sufficiently lightweight to perform real-time signal processing on up to four source and four target channels with recording from up to 128 channels running on a Windows 11 PC equipped with a 12th Gen Intel(R) Core (TM) i9-12900K processor and 64 GB of RAM. On startup, the VWM software preconfigures the Intan RHX software to initiate data collection and prepares the Intan controller hardware to receive stimulation triggers from the microcontroller via the I/O expander. The RHX software streams raw signals from 128 channels via a local TCP socket and transfers a user-defined subset of channels to the VWM software for real-time processing while also storing all data into dedicated files for optional offline analysis. TCP communication can, however, introduce unpredictable latencies and data packets can be received in different chunk sizes due to packet handling and operating system overhead. These latencies can degrade the communication of rate-encoded spike data between the source and target MEAs (62,63). To mitigate these issues,

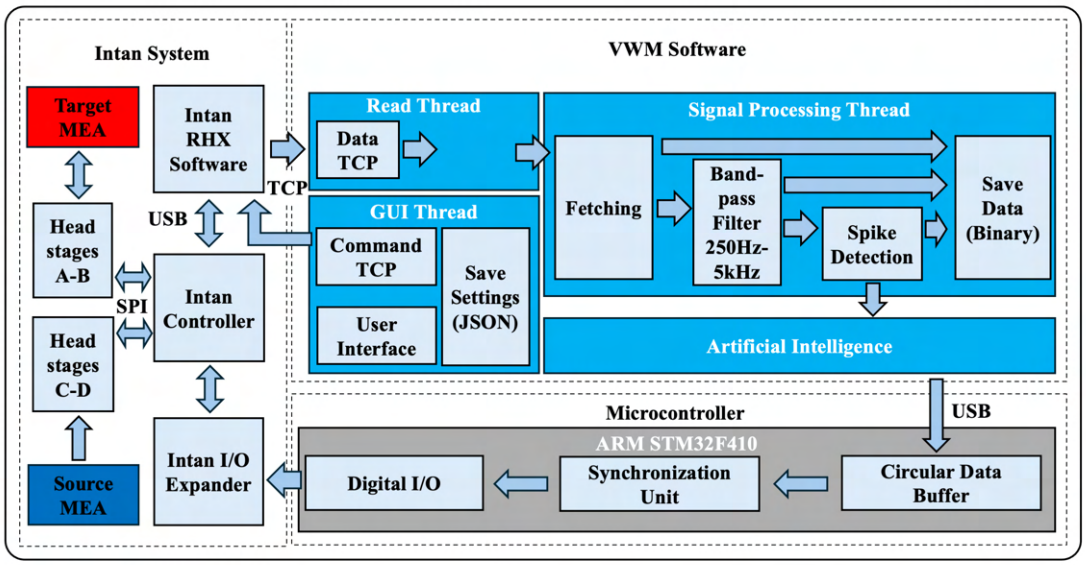

Figure 9 Block diagram of the Virtual White Matter (VWM) at software level.

the VWM software uses a circular data buffer. Namely, raw signal data is asynchronously pulled by the read thread and written into the circular buffer in variable-sized chunks as received via TCP. The signal processing thread then retrieves the data from the circular buffer in fixed chunk sizes, equivalent to 25.6 ms of data, ensuring consistent processing times and minimizing the effects of irregular delays between consecutive data chunks. The signal processing thread applies a user-defined band-pass Infinite Impulse Response (IIR) filtering (250-5000 Hz, Butterworth, 3rd order) followed by a custom spike detection module (see Section Realtime Spike Detection). Spike times were passed to the artificial intelligence (AI) module, which can be programmed to only trigger stimulations (see Section Stimulation) in the target MEA when source spikes meet certain user-defined criteria (e.g., channels 1 and 7 fire within 25 ms). For testing purposes, the AI was configured as a pass-through, meaning that every detected source spike triggered a matching stimulation in the target MEA.

2.4 Realtime Spike Detection

A real-time multi-threshold window discriminator spike detection system was created for the MEA signals observed in our dissociated neuron preparations. Conventional single-threshold spike detection algorithms, including the one used natively by the Intan RHX software, classify any signal crossing a fixed amplitude threshold as a spike. This approach is susceptible to post-stimulus artifacts, which can exceed the threshold without representing a true biological action potential, leading to false detections that would corrupt the cross-dish communication logic of the VWM system. To overcome this limitation, a custom double-threshold algorithm was developed that imposes additional temporal and morphological criteria to distinguish genuine action potentials from artifacts. The algorithm continuously monitors incoming data, identifying potential spikes when a signal crosses a negative threshold (-A) and subsequently a positive threshold (+B). If the time between these crossings is less than T1 or greater than T2, the event is classified as an artifact. Otherwise, the system waits for the signal to cross the zero. If the zero-crossing time falls within the range of T3 to T4, the event is classified as a spike, and as an artifact otherwise. Furthermore, the signal must not exceed ±C within a 1-millisecond window prior to crossing -A and 2 ms after. Some examples of the spike detections and artifact removals have been illustrated in Figure 10A.

All the above-mentioned parameters, namely, spike detection thresholds and time windows, were determined by an offline meta-analysis of data previously collected from six MEA preparations of E18 rat dissociated cortical neurons. In more detail, a simple threshold (4 times the background RMS level) was used to detect events, which were in turn reduced using PCA and clustered using K-means. Clusters of spikes were

differentiated from clusters of artifacts and noise and used as templates for tuning the spike sorting parameters A, B, C, T1, T2, T3, and T4. Results were consistent across all six MEAs. Threshold A and B were set, respectively to, 5.5 times and 2 times the background RMS of each channel. RMS levels for each electrode were determined over a 4-second period at the start of the experiment. Threshold C was fixed at ±70 µV, with T1, T2, T3, and T4 set to 0.2 ms, 0.6 ms, 0.25 ms, and 1 ms, respectively. These values were chosen based on the experimental setup and cell types and may vary under different conditions. It is important to note that in the target dish, the stimulus-induced responses predominantly manifested as bursting activity, which did not exhibit the typical morphology of individual

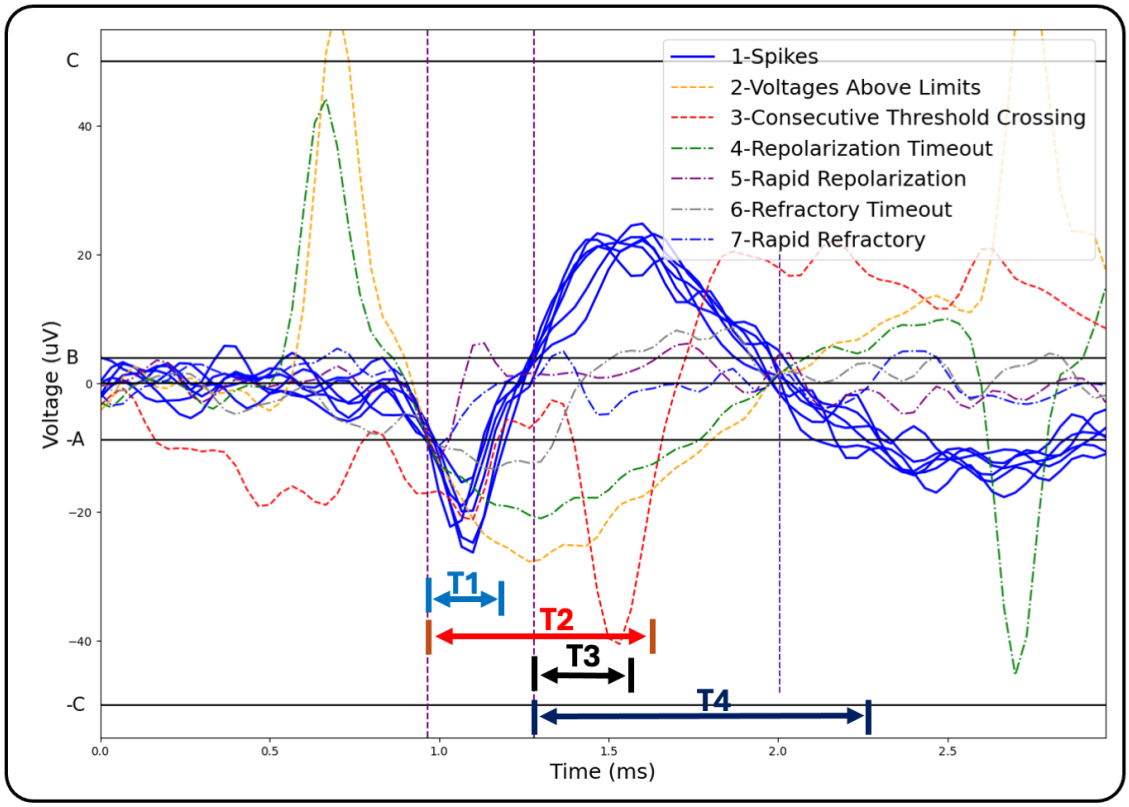

Figure 10 Spike detection technique. Illustration of the proposed double-threshold spike detection algorithm, showing representative waveforms classified into seven categories: true biological spikes (blue, AP[i] = 1), voltages above limits (yellow, AP[i] = 2), consecutive threshold crossings (red dashed, AP[i] = 3), repolarization timeout (green dash-dot, AP[i] = 4), rapid repolarization (purple dash-dot, AP[i] = 5), refractory timeout (gray dash-dot, AP[i] = 6), and rapid refractory (dark green dash-dot, AP[i] = 7). Thresholds A, B, and C and timing windows T1–T4 define the detection and artifact rejection criteria.

spikes. Unlike conventional spikes, the shape of spikes within bursts is more variable and less defined, making them less suitable for the proposed algorithm, which performed better with distinct individual spikes. To address this, both the proposed spike-detection algorithm and a simpler single threshold-crossing approach were tested to detect and analyze stimulation-induced responses.

2.5 Stimulation

To deliver stimulation patterns to the Intan head stages, two primary methods can be employed. The first is to send stimulation commands through the TCP Command Port. Testing revealed that the delays associated with this method due to transmission through the TCP Command Port, Intan RHX software, and the universal serial bus (USB) were inconsistent. To achieve consistent delays, a second method was developed in which stimuli were digitally triggered through the I/Os of the Intan expansion box. This method required the use of an STM32F407 microcontroller, receiving stimulation commands through USB, with an onboard circular buffer implemented to compensate for any timing inconsistencies in data recording or software-based signal processing. The circular buffer allowed asynchronous data input and synchronous output, ensuring precise timing.

Prior to stimulation, the VWM software preprograms the stimulation parameters—including pulse shape, amplitude, pulse width, number of pulses, etc.—into the Intan controller. The stimulation trigger of each target electrode is assigned to a digital input signal on the Intan expansion box. The microcontroller generates these triggering pulses based on the commands received from the VWM software via USB in real time. Each rising edge of a pulse on the expansion box's digital input activated the preprogrammed stimulation on the corresponding electrode, with the expansion box relaying the stimulation

triggers to the Intan controller. This entire synchronization process occurred within the firmware of the microcontroller and the Intan system, avoiding variability associated with operating systems and ensuring consistent timing. The final stimulation commands were transmitted to the headstages via Serial Peripheral Interface (SPI) cables.

Prior to running the VWM, a parameter optimization process was carried out to select the best stimulation parameters and target electrodes. This preliminary step ensured that the chosen parameters would robustly evoke post-stimulation activity while minimizing the risk of deleterious effects due to excessive or unbalanced charge density. A custom software tool called NeuroTuner was developed, interfacing with the Intan system via TCP. This tool facilitated systematic sweeps of stimulation across all electrodes on the MEA with different parameters, and data was recorded for offline analysis. The optimization process involved a symmetrical biphasic pulse sweep, starting with a current of 1 μA and a pulse width of 100 μs, which were systematically increased to find the optimal combination. Our analysis identified a current of 10 μA with a pulse width of 500 μs for each phase as optimal, consistently generating adequate post-stimulation biological spikes while maintaining cell viability.

With the optimal parameters set, an electrode sweep was performed on each MEA by NeuroTuner to identify the most suitable target electrodes. The most effective electrodes were selected based on their higher neural activity levels post stimulus, physical distance from each other, and the presence of viable cells, as confirmed by microscopic imaging. On the other hand, source electrodes were selected based on noise RMS, spontaneous spike rate, and impedance. Electrodes with acceptable impedances (below 200 kΩ) were chosen, as higher impedance increases noise levels, often exceeding spike voltages, making spike

detection impractical. The two electrodes with the lowest noise, highest spike activity, and acceptable impedance were chosen, ensuring independent and representative data collection. This careful selection process enhanced the reliability and quality of the recorded neural signals for analysis. Simultaneously, data from all 64 electrodes of the target MEA was recorded. Electrodes with impedance exceeding 200 kΩ or lacking significant activity post-stimulus were excluded from the analysis. This refinement resulted in 32 "active electrodes" being included for further analysis, enhancing the reliability and quality of the recorded neural signals.

To minimize stimulation-induced artifacts and amplifier railing—which occurs when stimulation voltages exceed the system's maximum readable voltage (6.4 mV for the Intan RHS system)—some neural recording devices offer blanking hardware features, namely the capability to completely turn off the amplifier and zero out the recording for a predefined time both pre- and post-stimulus to reduce artifacts caused by stimulation. However, this approach could potentially destabilize IIR filters due to DC-offset issues during the initiation phase following the zero-out period. Since this feature is not available in the Intan system, an alternative method was employed to address these artifacts. The Intan system was configured to temporarily reduce the amplification gain across all electrodes of the stimulated head stage during the stimulation. While a low-pass filter (with Intan's default setting at 1000 Hz) is commonly used to filter out these high-frequency artifacts, it proved impractical because the initiation of the filter prior to stimulation introduced start-up artifacts, especially in the presence of residual DC voltage from previous stimulations. By instead reducing the amplification during stimulation, these issues were mitigated, leading to more accurate signal detection and reduced artifact impact

(61). The current controlled stimulation method has been employed for stimulations. Current-controlled stimulation offers several advantages over voltage-controlled stimulation *in vitro* experiments. One significant benefit is its ability to provide more precise and consistent control over the amount of current delivered to the target tissue. This precision helps minimize the risks of tissue damage that can arise from the unpredictable variations in tissue and electrode impedance, which can affect voltage-controlled systems. Due to the variations in the impedances of the electrodes, when stimulated through a voltage-controlled method, the amount of voltage delivered to the cell or tissue will not be the same for all the electrodes, making the results dependent on the electrode impedance. Additionally, current-controlled stimulation can achieve more uniform and reliable activation of neurons, which is crucial for the effectiveness of the experiments. This uniformity enhances the reproducibility of neural responses and can improve the overall outcomes of neuromodulation studies. The adaptability of current-controlled systems also facilitates more accurate dose-response relationships, enabling better customization of stimulation protocols to meet the experimental requirements (64,65).

2.6 Parameter Optimization

Optimizing stimulation parameters to evoke sufficient post-stimulation activity while preserving cell viability is critical to this project. Excessive stimulation currents can lead to cell depolarization or irreversible damage, while insufficient currents may fail to elicit significant neural activity. The key factor in effectively evoking cellular responses is the amount of charge delivered to the cells, measured in microcoulombs (μC), determined by the product of current and pulse width. To achieve this balance, we developed a software tool, NeuroTuner shown on Figure 11, which interfaces with the Intan RHX Software via

TCP. NeuroTuner enables precise configuration of stimulation paradigms and systematic electrode sweeps, as illustrated in Figure 8. Initial optimization involved symmetrical biphasic pulse sweeps with pulse widths ranging from 100 µs to 1000 µs and pulse amplitudes from 1 µA to 20 µA. Analysis identified a current of 10 µA with a pulse width of 500 µs as the optimal combination, consistently generating adequate post-stimulation spikes while maintaining cell viability.

With the optimal parameters set, an electrode sweep was performed on each MEA by NeuroTuner to identify the most suitable target electrodes. The most effective electrodes

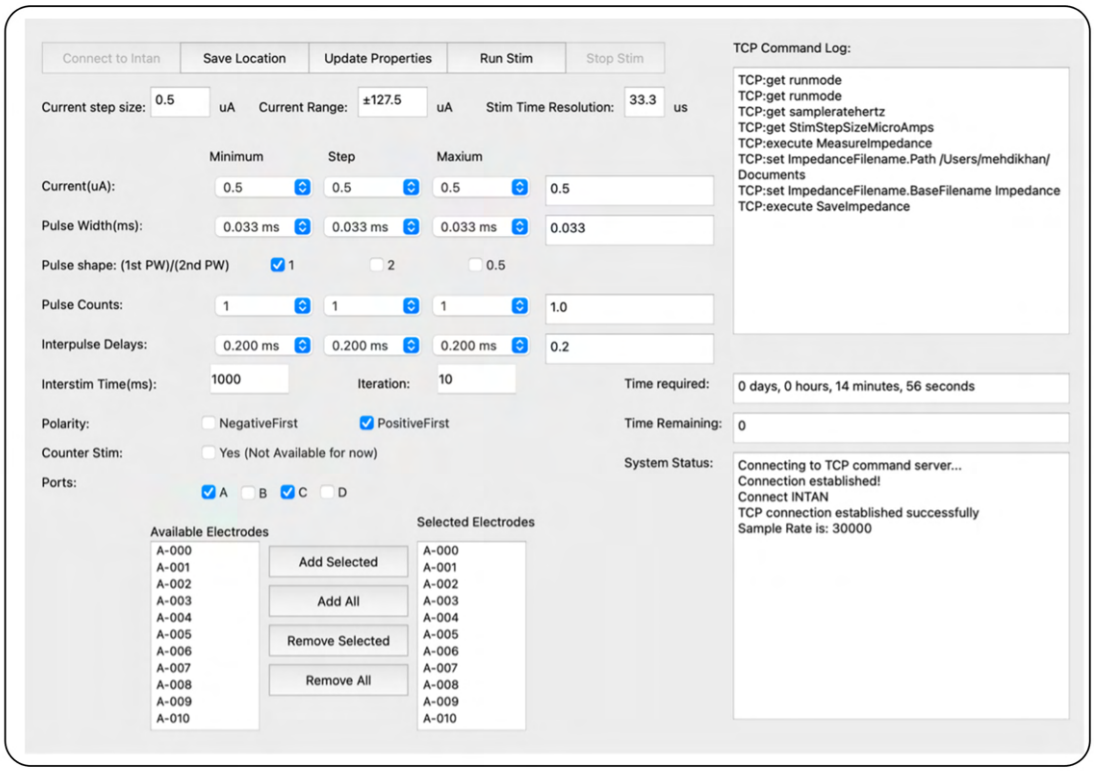

Figure 11 NeuroTuner graphical user interface for programmable electrical stimulation of neural preparations. The software enables full customization of stimulation parameters — including current amplitude (µA), pulse width (ms), pulse count, interpulse delay, interstimulus interval, pulse shape ratio, and polarity — with minimum, step, and maximum values configurable for each parameter to support systematic parameter sweeps. Individual electrode selection and multi-port control (Ports A–D) allow targeted delivery across specific MEA channels. A TCP command log and real-time system status panel provide feedback on device connectivity and stimulation progress, with estimated and remaining session time displayed during protocol execution.

were selected based on their higher neural activity levels post stimulus, physical distance from each other, and the presence of viable cells, as confirmed by microscopic imaging. On the other hand, source electrodes were selected based on noise RMS, spontaneous spike rate, and impedance. Electrodes with acceptable impedances (below 200 kΩ) were chosen, as higher impedance increases noise levels, often exceeding spike voltages, making spike detection impractical. The two electrodes with the lowest noise, highest spike activity, and acceptable impedance were chosen, ensuring independent and representative data collection. This careful selection process enhanced the reliability and quality of the recorded neural signals for analysis. Simultaneously, data from all 64 electrodes of the target MEA was recorded. Electrodes with impedance exceeding 200 kΩ or lacking significant activity post-stimulus were excluded from the analysis. This refinement resulted in 32 “active electrodes” being included for further analysis, enhancing the reliability and quality of the recorded neural signals.

3 SPECIFIC AIM ONE

Aim 1: Develop a robust VWM platform for real-time cross-dish neural communication.

3.1 Description

The project's initial phase was to show the proof of the concept of the system and test its various functionalities. A simple forwarder system has been designed to detect the spikes from two source electrodes and stimulate two electrodes in the target dish. This initial design emulates interregional brain communication and serves as a basis for the future investigation of more sophisticated neural interactions.

Subsequently, we validated whether the detected spontaneous spikes and evoked responses were truly biological. This included applying MK-801 to block N-Methyl-D-aspartate (NMDA) receptor activity and confirm that the observed spikes were not due to noise or stimulation artifacts. We also tested the delay between spike detection and stimulation, which was set to 200 ms, and checked its consistency across trials.

To evaluate how well the system could distinguish between the two stimulation sites, we analyzed the post-stimulus spike activity across different electrodes in the target dish. We examined which time periods after stimulation contained the most useful information and found that the first 10 ms carried the strongest signal for classification. We also tested bidirectional communication, where each dish could send and receive signals from the other using the same 200 ms delay. This setup allowed us to observe feedback loops and test the system under more dynamic conditions, similar to real brain regions interacting.

3.2 Validation

To confirm that the spontaneous activity in the source dish and the stimulus-evoked activity in the target dish were biological, we used MK-801, an NMDA receptor channel blocker.

The blocker was applied to suppress neural activity and verify that the spikes observed before its introduction were indeed biological rather than noise or stimulation artifacts. MK801 selectively inhibits neural activity while preserving other conditions and signals, including noise and artifacts.

The blocker was administered to reach a final concentration of 85 μM in the media following data collection during the VWM experiments. Neural activity gradually diminished over the course of 30 minutes, eventually reaching a complete cessation. The VWM experiment was conducted to confirm that the neural activity detected in the source MEA represented true biological signals rather than noise. Afterward, the media was replaced, and the blocker was removed to allow recovery over 72 hours. Given MK801's reversible effects, a return of spontaneous activity was confirmed as expected, which indicated that the neural silence was due to the blocker and not from permanent cell damage, cell dislodgment from the MEAs, or other issues. The successful resumption of activity upon blocker removal confirmed the effect was indeed due to MK801. Furthermore, the same procedure was successfully implemented in the target dish to verify that stimulus-evoked neural activity was a true biological response rather than a stimulation artifact.

We evaluated the system's timing by analyzing delays between spike detection in the source dish and stimulation in the target dish, using data from the VWM experiments. After refining the spike detection algorithms and optimizing inter-thread and inter-system communication, we achieved consistent 200 ms delays from spike occurrence in the source dish to stimulation in the target dish. While the 200 ms delay can be adjusted, it was chosen based on typical neural processing times, such as reaction times to sensory stimuli (150-

250 ms) (66) cortical processing in sensory pathways (100-200 ms) (67), and feedback loops in motor control (around 200 ms) (68), which are common in neural integration and response.

A key objective for evaluating the VWM was to assess how distinct the neural activity evoked by stimulation at each of the two target electrodes was by examining the stimulation responses across various recording electrodes in the target dish. Given that stimulation in 2D MEAs can spread throughout the dish and potentially affect multiple regions similarly, it was important to evaluate the uniqueness of the evoked activity. We addressed this by analyzing Post-Stimulus Timing Histograms (PSTH) of detected spikes across different recording sites in the target dish, focusing on a 200 ms window following stimulation at each of the two target electrodes. This analysis helped determine the distinctiveness of the responses from the two stimulation sites.

We subsequently developed a machine learning model to classify the target electrode of delivered stimulations by analyzing spike timings from a combination of one or more active electrodes, with the two stimulus target electrodes as output labels. Spike times were binned in 1 ms intervals within a 200 ms window following each stimulation event, resulting in a matrix format compatible with machine learning for a VWM dataset spanning 26 minutes. To enhance computational efficiency and preserve data integrity, Principal Component Analysis (PCA) was applied to reduce dimensionality while retaining 95% of the variance (n_components = 0.95), and each binned feature was normalized using z-score normalization. To identify the most effective model for predicting the stimulated electrode in the source dish, using evoked responses from the target dish, we compared several machine learning algorithms, including K-Nearest Neighbor (KNN), Support Vector

Machines (SVM), and Random Forests (RF). The dataset was split with 80% allocated for training and validation and the remaining 20% for testing.

To ensure a fair and unbiased evaluation of the model, we addressed two key sources of bias in our analysis. First, the dataset was unbalanced, with one target electrode having more stimulations than the other, which could potentially influence model performance. Second, relying solely on a simple train-test split risked introducing uneven data representation. To mitigate these issues, we employed stratified 10-fold cross-validation, which preserves class distribution in each fold and ensures that the model is tested on a representative mix of data from both labels. We based our analysis on all data from the 32 identified active electrodes and subsequently evaluated various combinations of these electrodes to determine the optimal number of required electrodes to achieve satisfactory performance.

To address the presence of any unwanted stimulation artifacts, potentially erroneously detected as spikes, in our data, we applied both single-threshold and double-threshold algorithms for spike detection and tested the data from both methods using the same machine learning algorithms. For validation that responses were the products of biological activity (rather than artifactual), we used data from a target dish treated with the channel blocker MK-801, where stimulation occurred without any NMDA-mediated neural activity in the target dish. The analysis revealed that the double-threshold method effectively eliminated all artifacts from the feature set, whereas the single-threshold method allowed some artifacts to be present in the analysis. These findings demonstrate the effectiveness and robustness of our double threshold spike detection technique.

3.3 Results

The VWM system demonstrated the capability to create functional connections between distinct neural populations in separate MEA dishes by triggering precise stimulation based on detected spike activity. Key findings from the experiments are summarized as follows:

3.4 Spike Detection and Artifact Mitigation

Spike events satisfying the spike detection criteria were identified on source electrodes 0 and 1, triggering electrical stimulation on corresponding target electrodes with a consistent delay of 200 milliseconds. The temporal alignment between spikes and stimulations exhibited high consistency (see Figure 12). However, each stimulation generated artifacts on nearby electrodes, including those within the same head stage, the same dish, and even on adjacent dishes. The magnitude of these artifacts is influenced by factors such as electrode impedance, physical distance between electrodes, and the design of the headstage chip and PCB traces. This can be seen in Figure 12 in the artifacts observed on the target

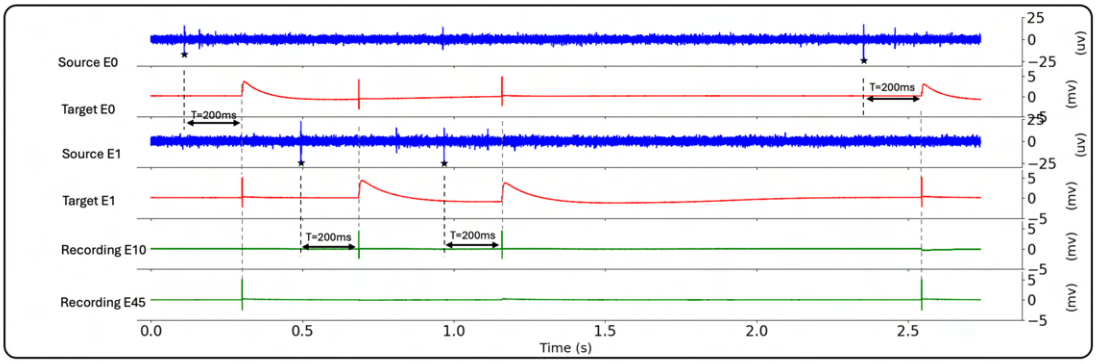

Figure 12 Representative multi-channel recording illustrating the closed-loop system operation over a 2.6-second window. Source electrodes E0 and E1 (blue, μV scale) display raw neural signals with detected spikes marked by asterisks. Each detected spike triggers a biphasic stimulation pulse delivered to the corresponding Target electrodes E0 and E1 (red, mV scale) after a fixed 200 ms delay. Recording electrodes E10 and E45 (green, mV scale) capture artifact propagation resulting from stimulation, confirming signal transmission across the target MEA while remaining outside the directly stimulated channels. Dual voltage scales (μV for source, mV for target and recording channels) are used to simultaneously visualize both the low-amplitude biological spikes and the orders-of-magnitude larger post-stimulus artifacts, which typically fall in the millivolt range.

electrodes as well as two randomly selected recording electrodes. When stimulation occurred on a headstage, a surge of electrical charge traveled through its SPI cable, creating a substantial electric field capable of interfering with nearby parallel cables. To mitigate this, we maintained at least 5 cm of separation between parallel cables. All recordings were conducted inside a grounded Faraday cage housed within a grounded incubator to minimize external electromagnetic noise.

3.5 Validation with MK-801

To validate the biological origin of the recorded neural activity, the NMDA receptor antagonist MK-801 was employed as a pharmacological control. Prior to drug application, spontaneous activity in the source dish was consistently detected and used to trigger stimulation in the target dish, producing robust stimulus-evoked neural responses (Figure 13A). Upon applying MK-801 to the target dish, evoked responses were markedly suppressed despite continued external stimulation, confirming NMDA receptor-dependent synaptic transmission as the underlying mechanism (Figure 13B). Removal of MK-801 and subsequent cell recovery restored post-stimulus spiking activity across target electrodes (Figure 13C), demonstrating the reversibility of the pharmacological blockade and confirming the sustained viability of the neural network throughout the experiment. Collectively, these results verify that the recorded signals reflect genuine biological neural activity rather than stimulation artifacts or non-specific electrical interference.

3.6 Post-Stimulus Spike Time Histograms

To achieve the VWM's objective of transmitting information across dishes, it was critical to demonstrate that stimulation at two distinct target electrodes could evoke discriminable neural responses at other electrodes on the MEA. Given that stimulation in 2D MEAs

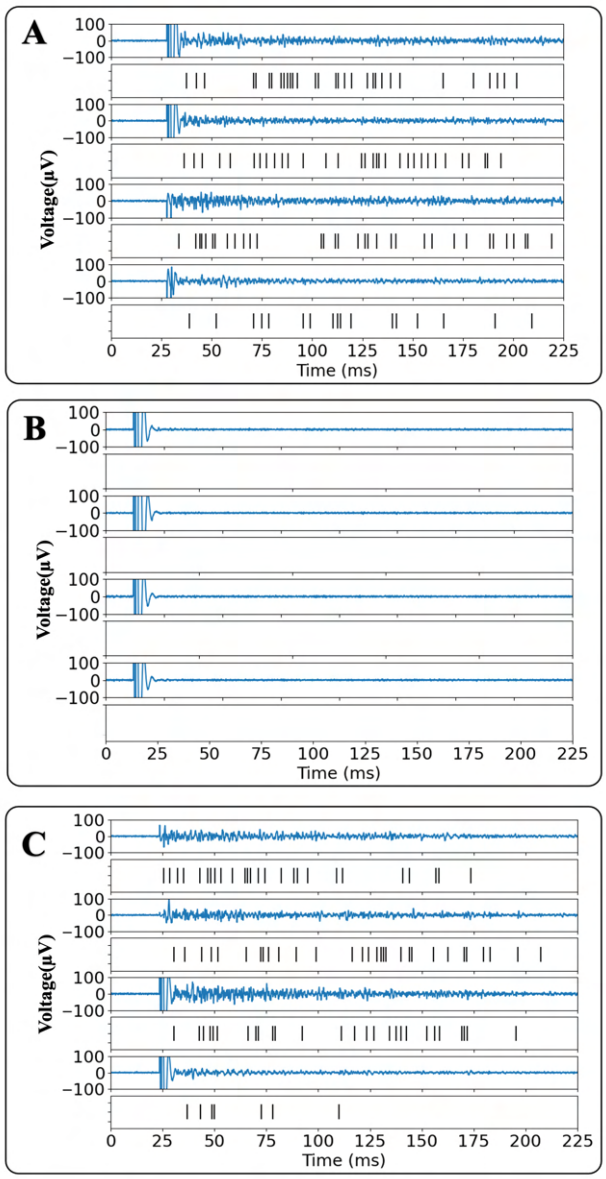

Figure 13 Post-stimulus high-pass filtered neural activity recorded from target MEA electrodes across three experimental conditions. Each panel displays voltage traces (μV) with corresponding spike raster plots over a 225 ms post-stimulus window. (A) Baseline activity recorded prior to pharmacological intervention, showing robust evoked spiking across multiple electrodes during intact network function under the virtual working memory (VWM) protocol. (B) Marked suppression of evoked activity following bath application of MK-801, an NMDA receptor antagonist, to the target dish, confirming glutamatergic synaptic blockade and demonstrating the NMDA-dependence of the observed network responses. (C) Partial recovery of evoked spiking activity following washout of MK-801 from both dishes and subsequent cell recovery, indicating reversibility of the pharmacological effect and sustained network viability throughout the experiment.

propagates and influences multiple regions simultaneously, it was essential to assess whether evoked post-stimulus activity was unique to each stimulation site. Demonstrating

this uniqueness would confirm that distinct information can be introduced into the neural preparation through targeted electrode stimulation. Conversely, if stimulation at different

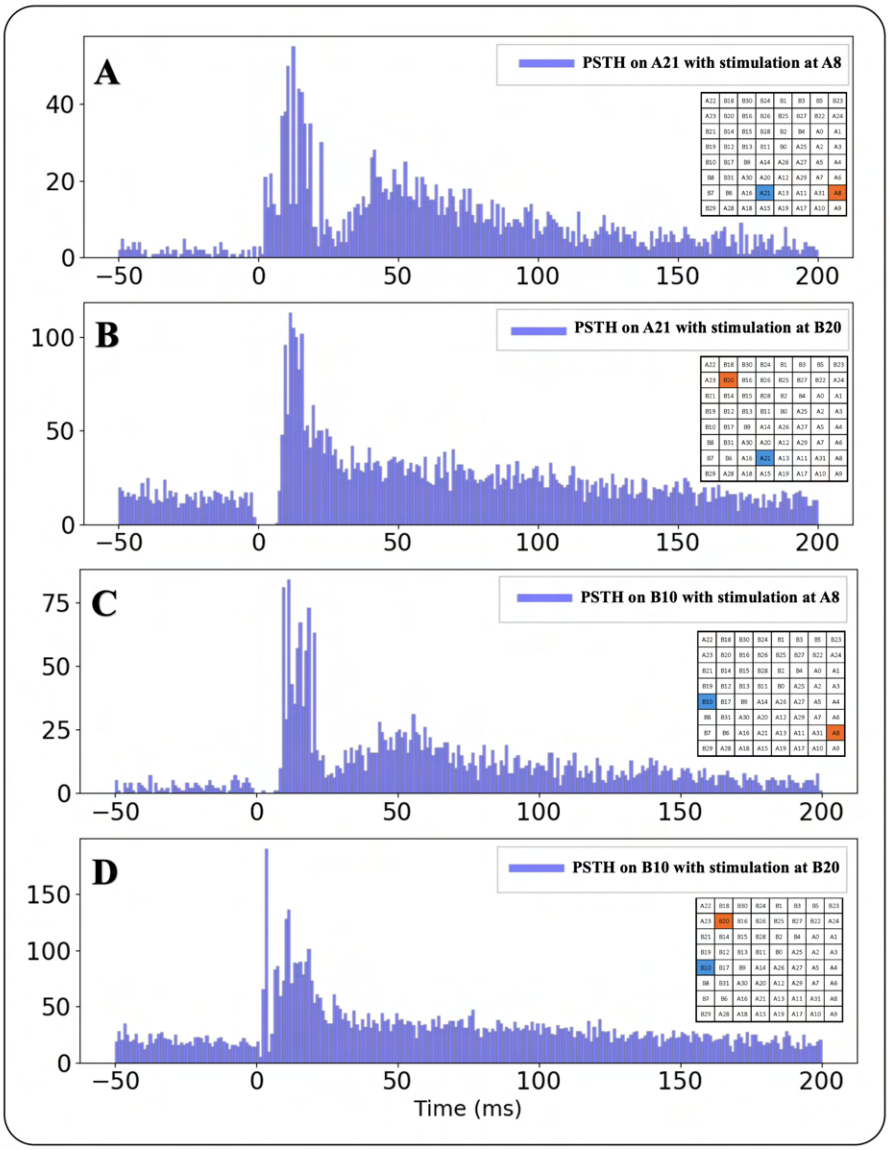

Figure 14 Post-Stimulus Time Histograms (PSTHs) depicting evoked neural responses recorded at two electrodes under two stimulation conditions. (A) Recording at A21 with stimulation at A8. (B) Recording at A21 with stimulation at B20. (C) Recording at B10 with stimulation at A8. (D) Recording at B10 with stimulation at B20. In each panel, the inset MEA map indicates the position of the stimulation electrode (red) and the recording electrode (blue). A pronounced increase in spike count is evident in the 0–50 ms post-stimulus window across all conditions, confirming evoked network responses. Notably, comparing panels A and B, where the same recording electrode (A21) responds differently depending on stimulation site, and similarly comparing C and D for electrode B10, reveals that the spatiotemporal profile of the evoked response is unique to each stimulation location. This spatial specificity in the histogram morphology and temporal dynamics supports the feasibility of machine learning-based spatiotemporal analysis to decode and distinguish the source of stimulation from multi-electrode recording patterns alone.

electrodes produced identical post-stimulus neural activity, the ability to differentiate input sources would be compromised.

To assess the uniqueness of evoked activity, post-stimulus spike time histograms (PSTHs) were analyzed within a 200 ms window relative to each stimulation electrode. Figure 14 presents PSTHs recorded from electrodes A21 and B10 in response to stimulation at target electrodes A8 and B20. Comparing panels A and B, both recorded at A21 but under different stimulation sites, reveals distinct differences in spike count magnitude and temporal distribution. The same pattern holds when comparing panels C and D at electrode B10. These differences in histogram morphology confirm that stimulation at spatially separate electrodes elicits distinguishable network-level responses, supporting the feasibility of encoding distinct inputs into the neural preparation and laying the groundwork for machine learning-based spatiotemporal decoding of stimulation source identity.

3.7 Artifact Removal

The efficacy of single- and double-threshold spike detection methods for rejecting stimulus artifacts were tested. Spikes detected from a combination of all active electrodes within 200 ms post-stimulus were used to train a machine learning algorithm to predict which of two electrodes had been stimulated. In the presence of MK-801, which silenced neural activity, the ML algorithms successfully differentiated between stimulus electrodes when trained with spikes detected using the single-threshold method. This indicates that, in the absence of biological activity, the stimuli were differentiable solely due to stimulation artifacts. In contrast, when trained using spikes detected with the double-threshold method

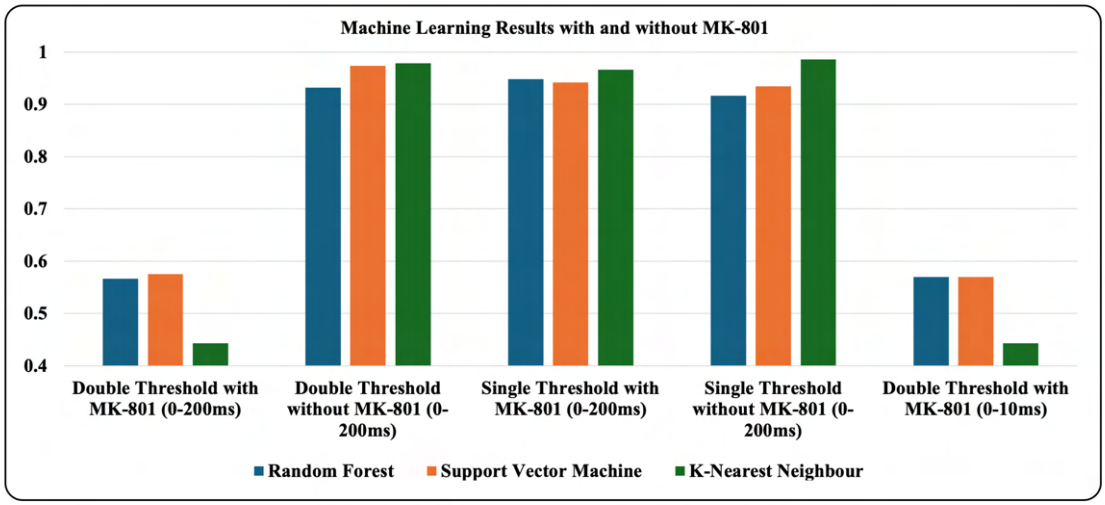

Figure 15 Comparison of machine learning classification performance across spike detection methods and pharmacological conditions. Random Forest (RF), Support Vector Machine (SVM), and K-Nearest Neighbors (KNN) classifiers were evaluated under five conditions: double threshold detection with MK-801 applied over a 0 to 200 ms window, double threshold detection without MK-801 over 0 to 200 ms, single threshold detection with MK-801 over 0 to 200 ms, single threshold detection without MK-801 over 0 to 200 ms, and double threshold detection with MK-801 over a restricted 0 to 10 ms window. Classification performance drops markedly in the presence of MK-801 across both detection methods, confirming that the classifier relies on genuine biologically driven neural responses rather than stimulation artifacts. The double threshold method without MK-801 and the single threshold method without MK-801 both yield high accuracy above 0.90 across all three classifiers, while conditions with MK-801 over the full window and the restricted 0 to 10 ms window produce scores near chance level, further validating the biological specificity of the evoked activity captured by the system.

under the same conditions, the differentiation between stimulus electrodes dropped to chance levels (accuracy around 0.5 Figure 15).

These results underscore the importance of rejecting stimulation artifacts in BNN or VWM preparations, as artifacts otherwise can mistakenly masquerade as transmitted information. Based on these findings, subsequent analyses exclusively utilized data from the double-threshold method to ensure artifact-free results. Although the double-threshold technique effectively isolates genuine neural activity, it may occasionally miss certain biological events, such as closely occurring neuronal spikes that deviate from typical spike shapes. Despite this limitation, the developed double-threshold method reliably distinguishes target electrodes while significantly minimizing the influence of artifacts based on the machine learning results shown on Figure 15.

3.8 Machine Learning Analysis

After validating the spike detection methods, machine learning techniques were applied to data collected without the MK-801 blocker, where both biological activity and stimulation were present. The analysis focused on classifying target electrodes using spike data recorded during the first 200 ms post-stimulation, as shown in Figure 16. Due to the combinatorial magnitude of analyzing all possible electrode combinations, random subsets of 100 combinations were generated and averaged for groups of 2, 3, 5, 10, 15, 20, 25, and 30 electrodes. For scenarios involving either a single electrode or all 32 active electrodes, the full set of possible combinations was evaluated, resulting in 32 and 1 combination(s), respectively. This approach ensured a balance between computational efficiency and analytical rigor, providing insights into how electrode numbers and selection affect

classification performance. The findings highlight the relationship between the number of electrodes used and the overall accuracy of the machine learning model.

To determine which electrodes and time frames provided the most valuable information for classifying stimulation targets, three metrics were applied: information gain, chi-square tests, and Fisher's score. These analyses, shown in Figure 17, identified the channels and time frames most critical for machine learning classification. In Figure 17, each section of the x-axis represents the 200 ms post-stimulus window for the specified active electrode,

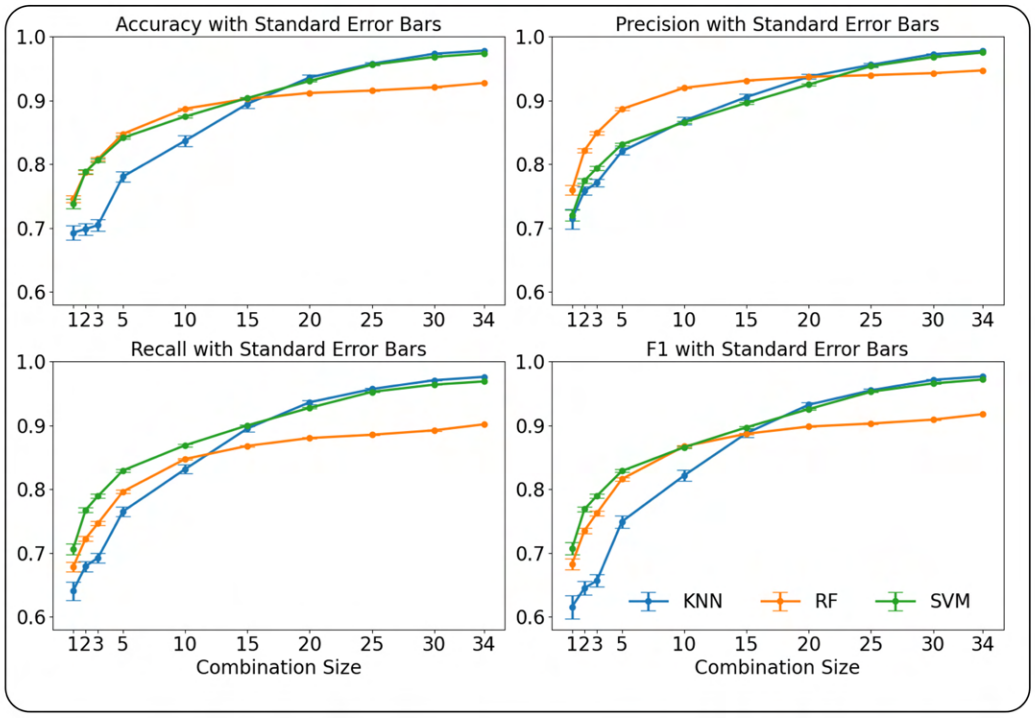

Figure 16 Machine learning classification performance as a function of electrode combination size, evaluated across accuracy, precision, recall, and F1-score metrics with standard error bars. Three classifiers, Random Forest (RF), Support Vector Machine (SVM), and K-Nearest Neighbors (KNN), were trained on 200 ms post-stimulus neural data to discriminate between stimulation sources. All three models show monotonically improving performance with increasing combination size, with SVM and RF reaching above 0.95 across all metrics at combination sizes of 25 and beyond. KNN demonstrates consistently lower performance at small combination sizes but converges toward comparable accuracy at larger electrode counts. Results indicate that spatiotemporal neural response patterns across as few as 10 to 15 electrodes are sufficient to achieve high classification accuracy, supporting the viability of electrode-based stimulation source decoding in 2D MEA preparations.

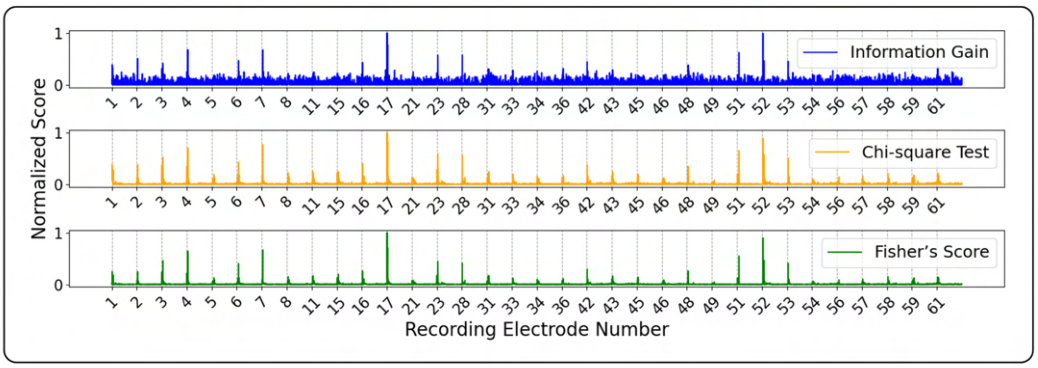

Figure 17 Normalized information richness scores across 62 recording electrodes computed using three statistical methods: Information Gain (blue), Chi-square Test (orange), and Fisher's Score (green). Each panel plots the normalized score per electrode over the 200 ms post-stimulus time window, reflecting the relative contribution of each electrode to stimulation source classification. Electrodes with consistently elevated scores across all three methods, notably electrodes 4, 7, 17, 52, and 53, represent the most informationally rich channels and are identified as the strongest candidates for main electrode selection in classification tasks.

and the y-axis reflects the importance scores assigned to each time point for each electrode. Notably, the large spikes at electrodes 17 and 52 indicate the special relevance of these two electrodes for decoding the source electrode.

Additionally, the peaks consistently occur within the first 10 ms of the post-stimulus window, highlighting the significance of this early time frame for classification and led to an investigation of how performance changes when using only specific portions of the early post-stimulation data. Various time frames, starting with the first few milliseconds after stimulation, were analyzed using data from all active electrodes. As shown in Figure 18 optimal performance was achieved when focusing on the first 10 ms of spike activity post-stimulation. Extending the analysis to longer time frames resulted in a decrease in accuracy, likely due to burst activity. During bursts, a large proportion of neurons synchronize their activity, which may confound the machine learning algorithms and obscure the differentiation between stimulation sources.

Additionally, illustrates the relationship between the number of electrodes used and

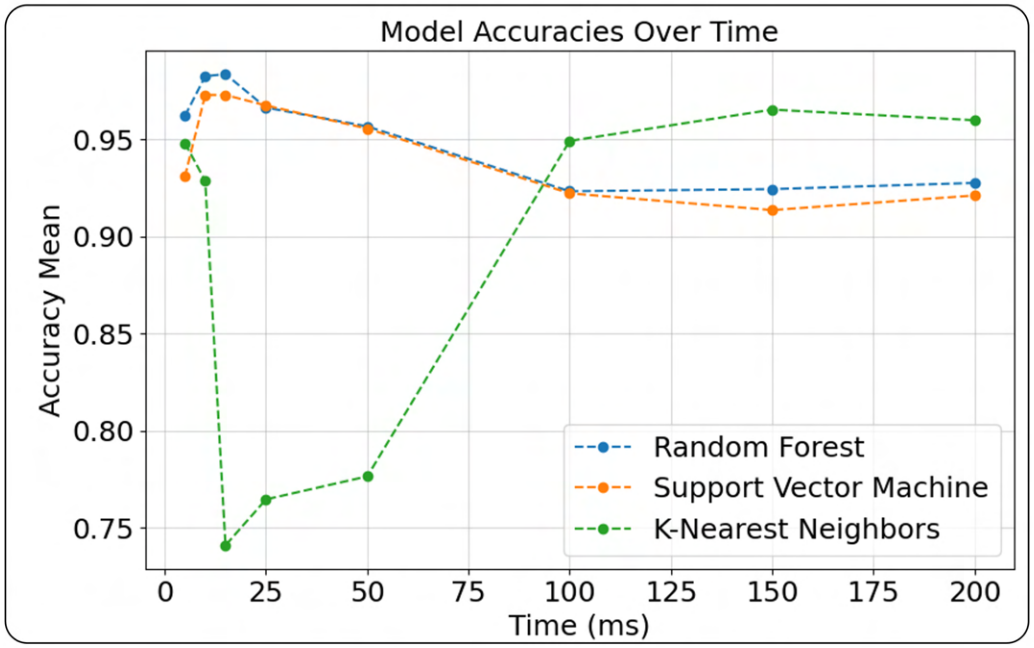

Figure 18 Mean classification accuracy over cumulative post-stimulus time windows for Random Forest (RF), Support Vector Machine (SVM), and K-Nearest Neighbors (KNN) classifiers. All three models achieve peak accuracy within the first 10 to 15 ms post-stimulus, with RF and SVM reaching approximately 0.98, indicating that the earliest evoked neural responses carry the highest discriminative information for stimulation source classification. KNN shows a pronounced accuracy drop between 15 and 25 ms before recovering and stabilizing above 0.95 by 100 ms, reflecting greater sensitivity to the temporal distribution of training data. RF and SVM maintain stable accuracy above 0.92 across the full 200 ms window, demonstrating robustness to the inclusion of later post-stimulus activity. These results highlight the informational dominance of early neural responses and suggest that classification pipelines focused on the initial post-stimulus period can achieve high accuracy with reduced computational demands.

classification accuracy for the 10 ms time frame. While the first 10 ms contained the most valuable information, reducing the number of electrodes also led to a decrease in accuracy, likely due to the smaller dataset available for training. Conversely, using more electrodes improved classification performance but with diminishing returns beyond a certain number of electrodes. These findings highlight the importance of early neural responses and comprehensive electrode coverage for accurate classification, providing insights into optimizing data collection and processing for future studies. Furthermore, we applied the

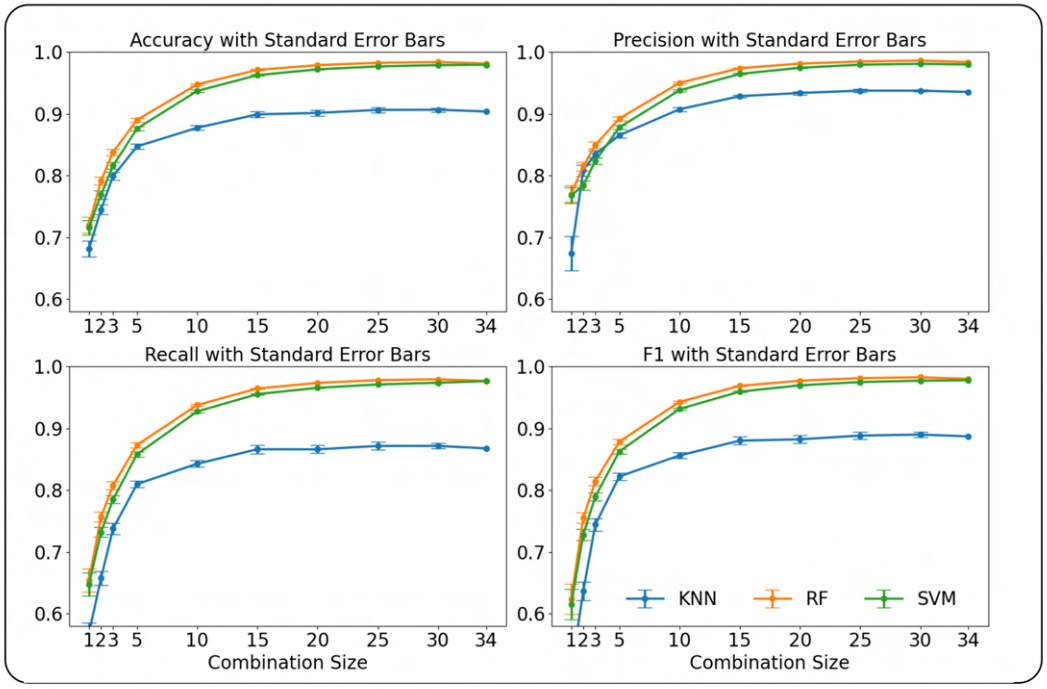

Figure 19 Machine learning classification performance as a function of electrode combination size, evaluated across accuracy, precision, recall, and F1-score metrics with standard error bars. Three classifiers, Random Forest (RF), Support Vector Machine (SVM), and K-Nearest Neighbors (KNN), were trained on 10 ms post-stimulus neural data to discriminate between stimulation sources.

same machine learning approach to data combined from all electrodes under MK-801 conditions in the target dish, using a doubled threshold within the 0–10 ms period. As shown in Figure 15, even focusing solely on the first 10 ms did not enhance accuracy when MK-801 was present. This outcome suggests that the improvements observed in other conditions are driven primarily by biological neural activity rather than stimulation artifacts.

Overall, the machine learning results demonstrate that using a traditional window discriminator double-threshold approach and 10 ms windows post-stimulus enables the system to introduce information into a neural preparation and extract information processed by the BNN. This neural processing holds immense value as it can be leveraged for diverse

applications, such as image processing, signal filtering, and other tasks where BNNs can interpret and relay information between neural systems.

3.9 Bidirectional Connection:

A key feature of the VWM platform is its ability to establish real-time bidirectional communication between two independent neural cultures on separate MEAs as shown in Figure 20. This capability allows the system to model the reciprocal interregional communication observed in biological neural circuits, where most brain regions are

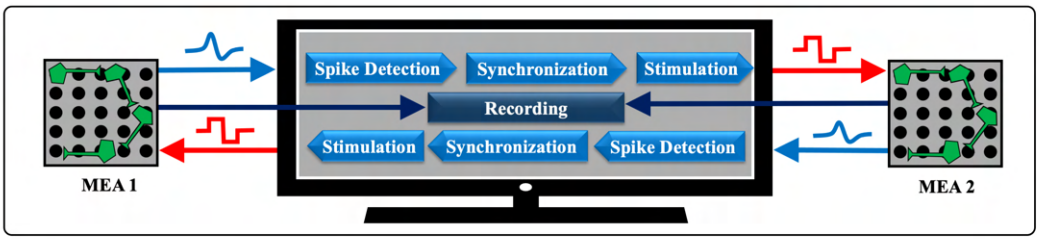

Figure 20 Schematic overview of the proposed bidirectional closed-loop MEA system. Neural signals recorded from MEA 1 undergo real-time spike detection and synchronization processing, triggering a corresponding stimulation waveform delivered to MEA 2, while simultaneously, signals recorded from MEA 2 undergo the same pipeline to drive stimulation back to MEA 1. A continuous recording feedback loop running between both preparations through the central computing interface enables simultaneous, adaptive, bidirectional communication between the two neural networks.

interconnected in a bidirectional manner. In the current proof-of-concept implementation, spikes detected from either MEA trigger stimulation on the other MEA after the same fixed delay of 200 ms. Each MEA includes two dedicated electrodes for spike detection and two separate electrodes for stimulation. The same spike detection algorithm is applied symmetrically to both networks, enabling fully reciprocal closed-loop interactions without any gating or filtering of the stimulation events.

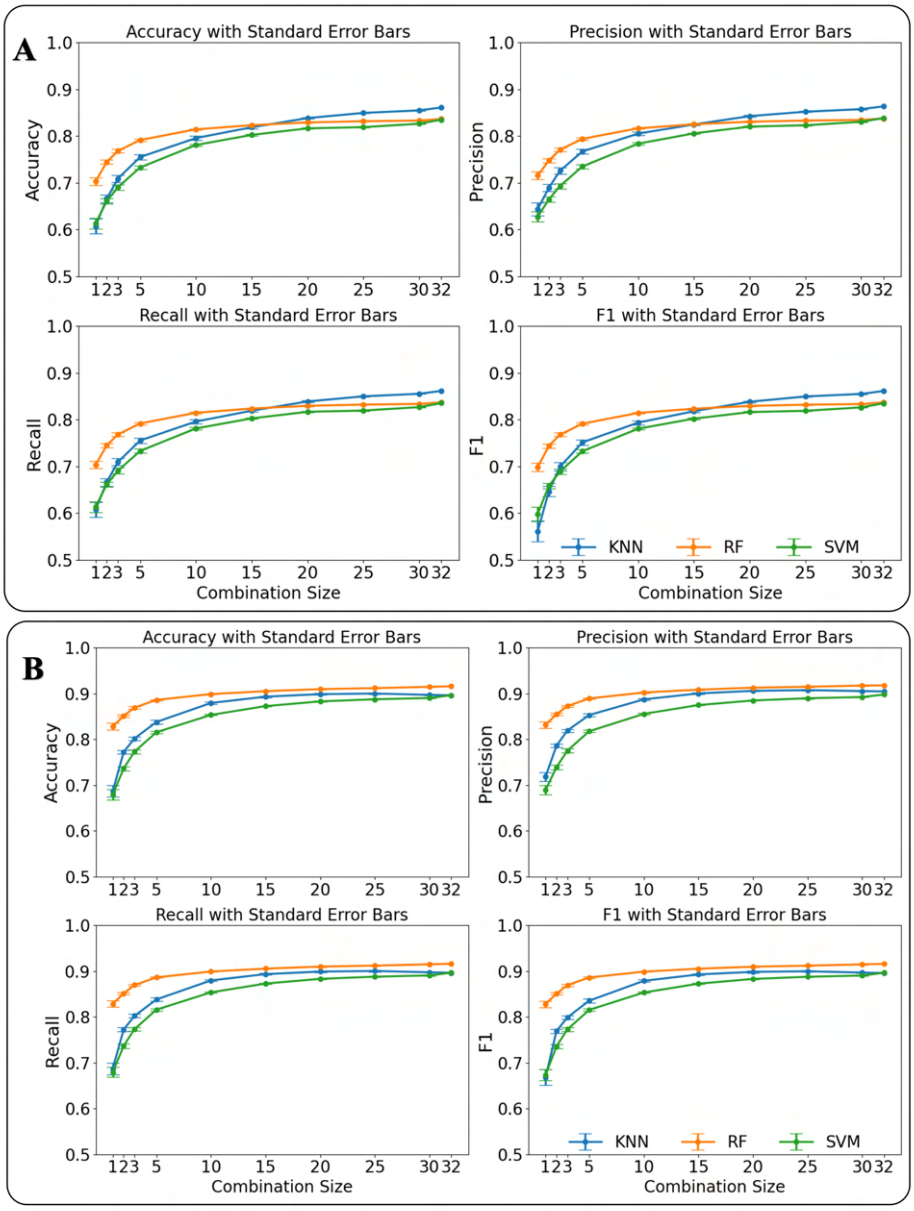

Figure 21 Machine learning classification performance as a function of electrode combination size in the bidirectional VWM setup, evaluated across accuracy, precision, recall, and F1-score metrics with standard error bars. Three classifiers, Random Forest (RF), Support Vector Machine (SVM), and K-Nearest Neighbors (KNN), were assessed under four conditions using 32 selected electrodes. (A) Classification results for MEA1 based on 200 ms post-stimulus activity, with all three classifiers reaching approximately 0.85 at the maximum combination size. (B) Classification results for MEA2 based on 200 ms post-stimulus activity, showing higher overall performance with RF and SVM converging above 0.90.

This unrestricted bidirectional configuration was designed to explore emergent network dynamics and information flow between dissociated neural populations. However, one

observed consequence is the formation of positive feedback loops, where stimulation on one MEA evokes activity that subsequently triggers stimulation on the other MEA, potentially resulting in self-sustained excitatory activity. These feedback loops can lead to

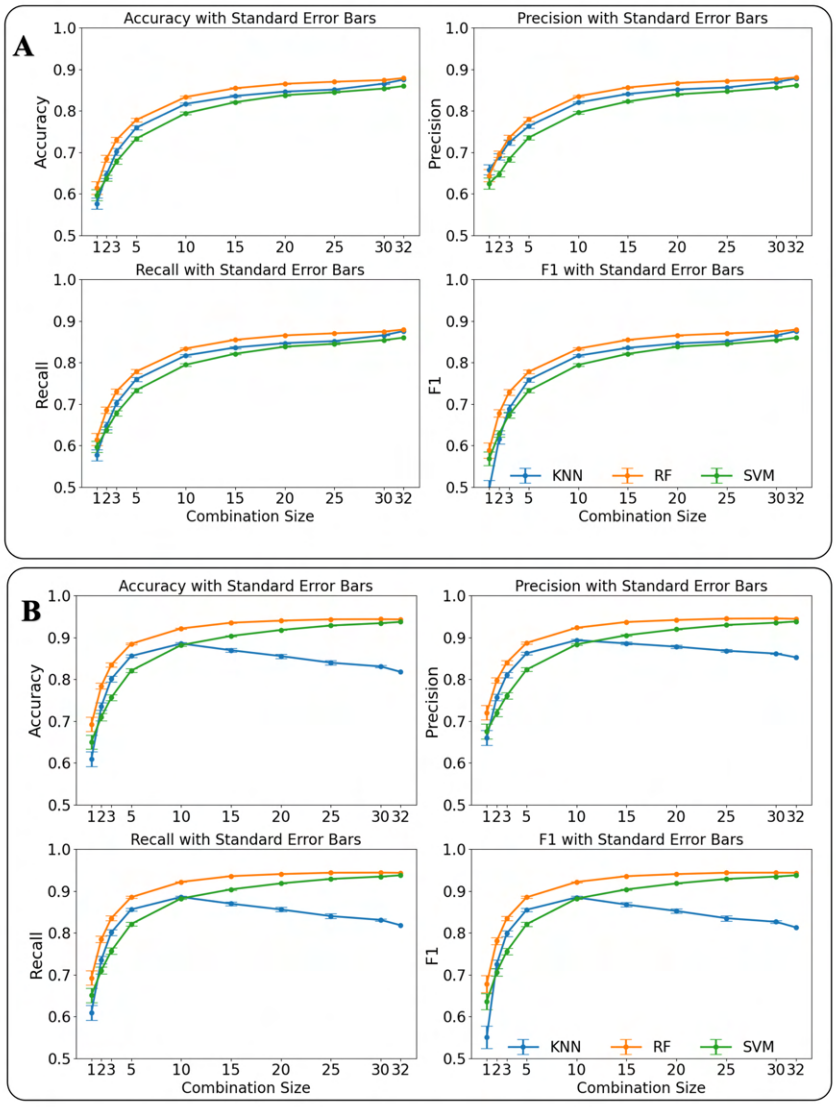

Figure 22 Machine learning classification performance as a function of electrode combination size in the bidirectional VWM setup, evaluated across accuracy, precision, recall, and F1-score metrics with standard error bars. Three classifiers, Random Forest (RF), Support Vector Machine (SVM), and K-Nearest Neighbors (KNN), were assessed under four conditions using 32 selected electrodes. (A) Classification results for MEA1 based on 10 ms post-stimulus activity, demonstrating comparable performance to the 200 ms window despite the substantially reduced time frame. (B) Classification results for MEA2 based on 10 ms post-stimulus activity, with RF and SVM surpassing 0.93 across all metrics at larger combination sizes, while KNN plateaus near 0.85. Across all conditions, performance improves monotonically with increasing electrode combination size, and the 10 ms window results confirm that early post-stimulus neural activity retains sufficient discriminative information for high-accuracy classification in a bidirectional network configuration.

excessive stimulation, which in turn induces a temporary reduction in neural activity due to depolarization block—a phenomenon in which prolonged or intense stimulation inhibits neuronal firing temporarily (69,70). Notably, this suppression is reversible, with spontaneous activity typically resuming a few seconds after stimulation ceases.

To evaluate the system's classification performance under bidirectional conditions, machine learning models were trained independently for each MEA using post-stimulus activity from 32 selected electrodes over a recording duration of 12 minutes. Results for the 200 ms analysis window are shown in Figure 21A for MEA1 and Figure 21B for MEA2, while results for the 10 ms analysis window are presented in Figure 22A and Figure 22B respectively. Overall performance was slightly lower compared to the unidirectional configuration, likely due to overlapping stimulation events caused by positive feedback loops. These overlaps within the analysis window obscured distinct evoked response patterns, diminishing the models' ability to accurately classify the stimulation source. However, similar to the unidirectional VWM, the 10 ms post-stimulus data yielded slightly better results than the 200 ms data, as shorter windows reduced the likelihood of additional overlapping stimulations.

4 SPECIFIC AIM TWO

In the second phase of the VWM experiment, as shown in Figure 23, the VWM platform was extended to enable structured binary communication between dissociated cortical cultures in physically separate MEA dishes. Throughout all experiments, the two communicating neuronal networks were maintained in physically separate MEA dishes, each containing an independent dissociated cortical culture with no shared substrate. All decoding therefore reflects cross-dish, not intra-network, signal propagation. In this context, "structured" refers to the use of predefined binary patterns (sequences of 0s and 1s) rather than arbitrary or spontaneous neural activity, enabling systematic evaluation of information transfer fidelity.

The top-level system block diagram is shown Figure 23. The overall goal is to transmit a three-bit data word from one neural culture (MEA 1) to a second one (MEA 2), and then back again to the first one in real time. This will set a benchmark for quantifiable transmission and bit error rates between neural cultures. A pair of stimulation electrodes was assigned in each MEA, with one electrode representing binary “0” and the other representing binary “1.” A series of 3-bit words were encoded by delivering sequential electrical pulses to the corresponding electrodes, with a fixed 1-second interval between

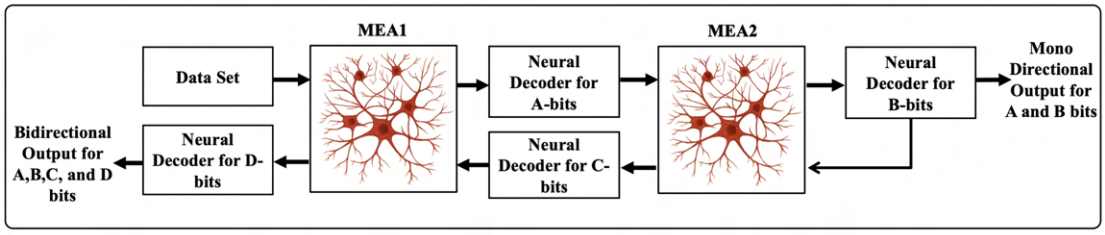

Figure 23 Monodirectional and Bidirectional Neural Transmission Architectures. A Closed-loop monodirectional and bidirectional communication protocol demonstrating real-time signal transmission between MEA 1 and MEA 2. Structured 3-bit binary data packets are delivered to the source MEA, decoded, error-corrected, re-encoded, and transmitted to the target MEA, enabling iterative decoding and transmission fidelity assessment across multiple stages.

bits to ensure that the neural network returned to a non-bursting baseline state before the next stimulation. A parity bit was appended to each word for error correction, forming a 4-bit transmission packet. A 2-second inter-word interval further reduced the chance of overlapping post-stimulation activity. The 1-s inter-bit and 2-s inter-word intervals were chosen to avoid stimulation-induced bursting and to allow network return to baseline. Pilot tests with shorter intervals produced overlapping evoked activity that degraded decoder accuracy. Stimulation pulses were current-controlled, charge-balanced, and biphasic, with a positive-first configuration of 10 μA amplitude and 500 μs phase duration, yielding a charge density of 2×10−4C/cm2 per phase.

A real-time machine learning model was employed to decode the transmitted bits, as described in Section 4.2. The decoding process identified the stimulated electrode corresponding to each bit based on the evoked activity recorded from six output electrodes selected in section 4.1. The feature set was constructed by time-binning action potentials from the selected output electrodes within the 0–200 ms post-stimulus window using 1 ms bins, thereby preserving the temporal resolution of spike timing. For each bit, the classifier provided both a predicted label and a confidence score. After decoding all four bits, the parity bit was used to verify the integrity of the transmission. Using an even parity scheme, the parity bit was expected to be 0 if the sum of the three data bits was even, and 1 if the sum was odd. If the parity check failed, the bit with the lowest classification confidence—including the parity bit—was toggled to correct the error. This corrected data word, along with a newly computed parity bit, was then used to stimulate the second MEA. The corrected 3-bit data word, along with a newly computed parity bit, was then re-encoded and transmitted to the second MEA using the same stimulation protocol. The decoding and

error correction process was repeated at the receiving end, completing the mono-directional communication scheme. The original encoded message was compared with the decoded outputs from both MEAs to evaluate transmission fidelity and error correction performance.

To emulate bi-directional communication observed in biological systems, the next phase of the experiment involved sending the decoded and parity-corrected data from the second MEA back to the first MEA. This step completed a real-time closed-loop communication pathway. The decoded word from MEA 2 was re-encoded and delivered as patterned stimulation to MEA 1. This reverse transmission followed the same encoding, stimulation, and decoding protocol. The final decoded output at the first MEA was compared to the original message, enabling performance evaluation across each stage of the round-trip transmission. These comparisons provided quantitative benchmarks for bit-level accuracy, error correction efficacy, and overall system reliability. To assess the contribution of machine learning to decoding performance, a comparative experiment was conducted using a traditional spike integration and thresholding approach, as shown in Figure 24.

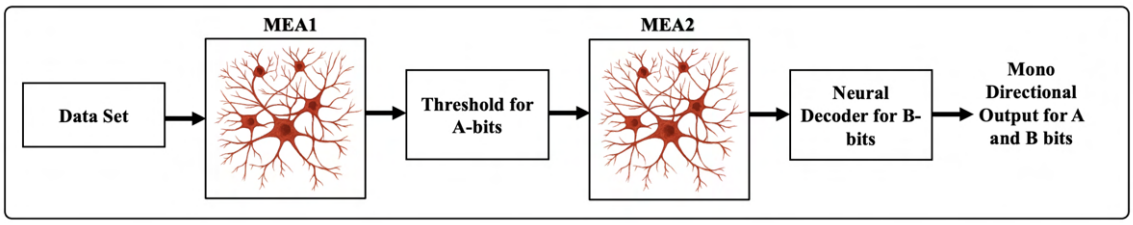

Figure 24 Threshold-Based Neural Transmission Architectures. Alternative monodirectional configuration replacing one of the machine learning classifiers with spike count integration and threshold-based detection. This approach provides a baseline for evaluating decoder performance against ML-based methods.

4.1 Electrode Selection

The performance of the neural data transmission framework depends on the selection of two input electrodes (used for stimulation) and six output electrodes (used for decoding via machine learning). To identify the most effective combination, a systematic two-phase approach was developed. In the first phase (shown in Figure 25) the objective was to identify two optimal input electrodes capable of reliably evoking widespread and distinct neural activity. Each electrode on the MEA was stimulated individually using a custom stimulation control tool. Following each stimulation, evoked spike activity was recorded across all electrodes. To quantify each electrode's impact on the network, evoked spikes on each electrode occurring within a 0–200 ms post-stimulus window were summed. Electrodes were ranked according to this evoked activity, and from the highest-ranked candidates, two spatially distant electrodes were selected as input channels for subsequent transmission experiments. To ensure topological diversity and minimize overlap in downstream activation, the two selected input electrodes were required to be separated by a minimum Euclidean distance of 600 µm (equivalent to 4 electrode spacings, given an

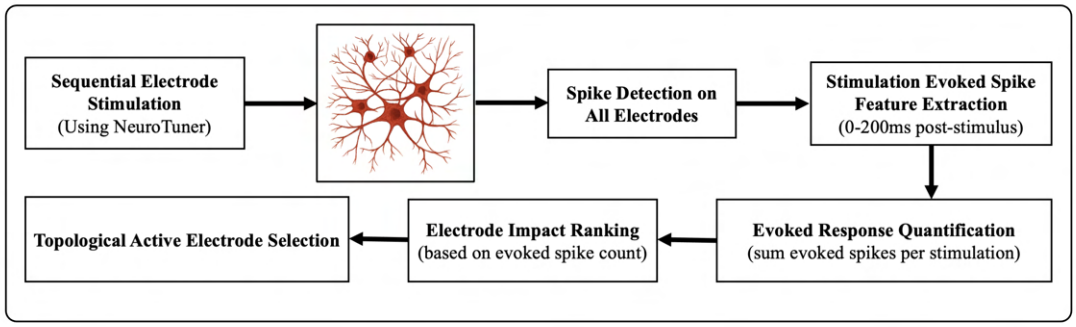

Figure 25 Pipeline for selecting input electrodes based on evoked network activity. Each electrode was stimulated individually using NeuroTuner, followed by spike detection across all recording channels. Stimulation-evoked spike features were extracted within a 0 to 200 ms post-stimulus window and summed per stimulation event to quantify each electrode's capacity to drive network-wide activity. Electrodes were subsequently ranked by their evoked spike count, and topological active electrode selection identified two top-performing, spatially distant electrodes for use as input channels, ensuring maximal spatial coverage and discriminability of evoked responses across the MEA.

inter-electrode distance of 150 µm). Concretely, once the highest-ranked electrode was identified, all electrodes falling within this radius were excluded from consideration, and the second input electrode was selected as the highest-ranked candidate outside this exclusion zone.

In the second phase (shown in Figure 26) a machine learning-based strategy was employed to identify a set of output electrodes (6 out of 64) capable of producing discriminable post-stimulation activity patterns. A randomized dictionary of 4-bit transmission packets—comprising 3-bit data plus a parity bit—was generated to encode stimulation sequences. Using this dictionary, the two selected input electrodes were stimulated sequentially, and spike activity was recorded across the MEA. For each stimulation event, a feature vector was constructed by discretizing the evoked spike train into 1 ms time steps across the 0–200 ms post-stimulus window. Each time step was assigned a binary value indicating the presence or absence of a spike, providing a high-resolution temporal representation of the electrode's response. To assess the discriminative capacity of each electrode, a machine

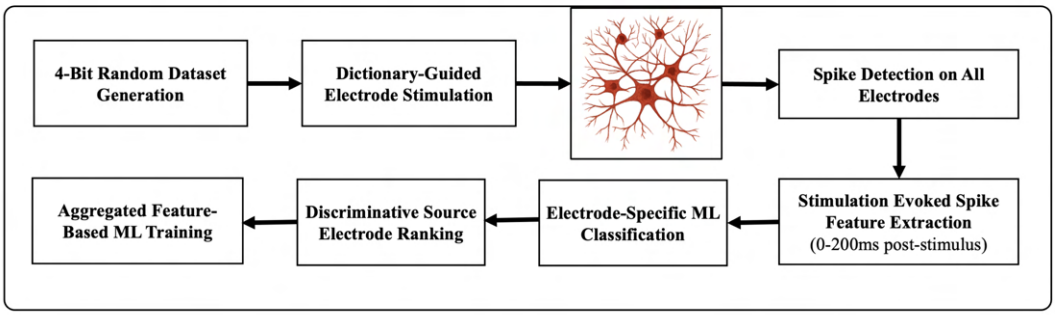

Figure 26 Pipeline for identifying discriminative source electrodes and training the machine learning classifier. A randomized dictionary of 4-bit transmission packets, comprising 3 data bits and a parity bit, was generated and used to drive dictionary-guided sequential stimulation of the two selected input electrodes. Spike activity was recorded across all electrodes following each stimulation event, and stimulation-evoked spike features were extracted by binning detected spikes within a 0 to 200 ms post-stimulus window using 1 ms bins. An electrode-specific machine learning classifier was then trained iteratively, evaluating each recording electrode individually as a candidate source based on its discriminative capacity. Electrodes were ranked by classification accuracy, and the six top-performing channels were selected. A final aggregated feature-based model was trained using the combined feature set from these six electrodes to optimize stimulation source identification performance.

learning classifier was trained iteratively using the binned features from each electrode as input. Classification accuracy was evaluated for each model, and the six electrodes yielding the highest performance were selected as the most informative sources. A final classifier was then trained offline using aggregated features from these top-ranked electrodes, forming the basis for the real-time machine learning model used in subsequent decoding tasks. Across preparations, preliminary analyses found that decoder accuracy saturated between 5–7 electrodes; selecting the top six provided a stable trade-off between performance and computational load while achieving consistency across datasets.

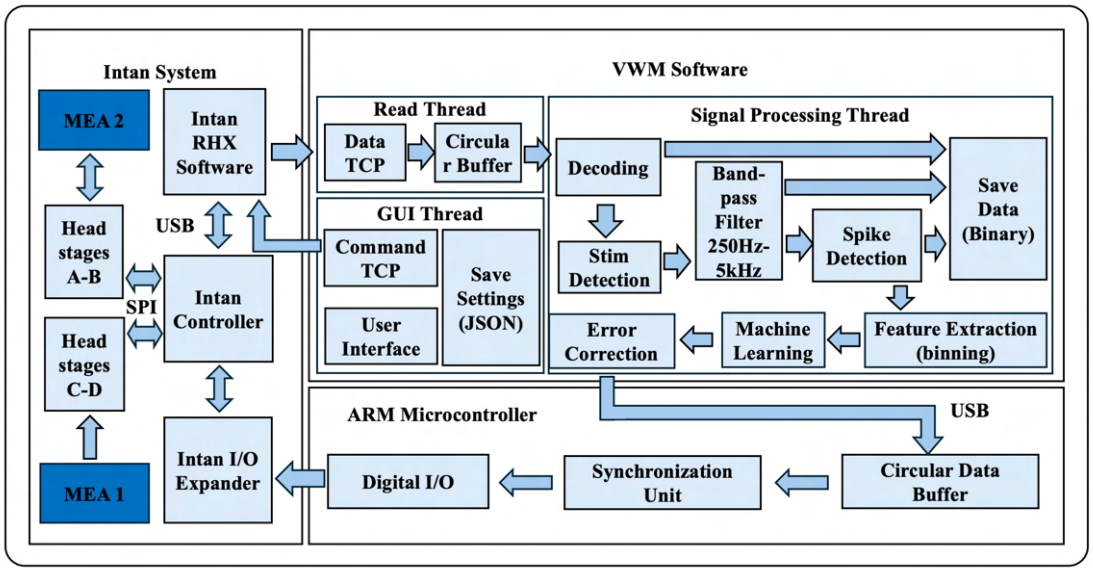

Figure 27 Detailed system architecture integrating hardware and software components for real-time neural communication between dissociated cultures. Neural activity is recorded simultaneously from MEA1 and MEA2 via Intan head stages (A-B and C-D), routed through the Intan Controller and I/O Expander over SPI, and streamed to the Intan RHX software via USB. Within the VWM software, a Read Thread receives raw data over TCP and buffers it in a circular buffer, while a parallel GUI Thread manages user interaction, command TCP communication, and JSON-based settings storage. The Signal Processing Thread performs sequential decoding, bandpass filtering (250 Hz to 5 kHz), stimulation detection, spike detection, feature extraction through binning, machine learning classification, and error correction, with processed data saved in binary format. Classified output is passed via USB to an ARM microcontroller, which buffers decoded data in a circular buffer, coordinates timing through a synchronization unit, and drives digital I/O signals to the Intan I/O Expander to deliver spatiotemporal stimulation patterns back to the MEAs. This closed-loop architecture supports both monodirectional and bidirectional neural communication with real-time decoding and transmission fidelity validation.

4.2 Machine Learning

The complete architecture is shown on Figure 27 in which feature vectors were extracted from binned spike trains by quantifying evoked responses within a 0–200 ms post-stimulation window using 1 ms bins, yielding a 200 × 6 binary matrix per trial, where rows represent time bins and columns represent the six preselected output electrodes, with each entry indicating the presence (1) or absence (0) of a spike in that bin on that electrode. Given that individual neurons can fire at intervals of only a few milliseconds, the 1 ms bin size was selected to preserve the temporal resolution of spike timing across electrodes.

To reduce variability in firing rates and temporal jitter, the binned spike counts were normalized using a per-channel z-score transformation. Although individual bin values are binary, z-scoring operates across the trial dimension for each electrode, rescaling each channel's response relative to its mean and standard deviation over the training set. Z-scoring was performed across the distribution of responses for each electrode over the entire training set, not within a single trial. This preserves trial-to-trial structure while removing global amplitude biases arising from electrode impedance variability or differences in tissue coupling. This is necessary because one stimulation electrode may consistently evoke more spikes than the other, due to differences in electrode-tissue coupling, electrode impedance, or tissue density around the electrode, which would otherwise allow the classifier to exploit absolute spike-count disparities rather than the underlying spatiotemporal response patterns. Z-scoring removes this bias and ensures the classifier operates on relative response structure.

Dimensionality reduction was performed via principal component analysis (PCA), retaining 95% of the total variance to streamline computation and improve classifier

performance. Because the proportion of variance captured by each component varies across experiments, the number of retained components was not fixed but determined independently for each session, resulting in a compact feature vector of variable dimensionality that was passed to the classifier. Together, electrode impedance drift, stimulus artifact variability, and spontaneous background firing constituted major sources of measurement variability, motivating both the use of fine 1-ms temporal binning to preserve precise spike timing and PCA-based dimensionality reduction to suppress unstructured noise while retaining shared spatiotemporal response structure.

Multiple classifiers were evaluated offline using stratified 10-fold cross-validation, including Support Vector Machines (SVM), Random Forests, and K-Nearest Neighbors, each tested with various input configurations. To ensure sufficient training data for model generalization, between 400 and 800 stimulations were used for training; smaller datasets (fewer than 400 stimulations) consistently led to poor generalization and unstable model performance, while larger datasets did not yield substantial improvements in cross-validation accuracy. Stratified 10-fold cross-validation was employed to evaluate model generalization on unseen data and guard against overfitting. Among the tested classifiers, the SVM with a sigmoid kernel ($C = 10$) consistently achieved the highest classification accuracy and was selected for real-time decoding. Aggregated binned spike features from six preselected output electrodes—previously shown to be sufficient out of the full 64-electrode array to achieve acceptable classification performance (71)—were used to train the final SVM model. The trained classifier, along with the fitted z-score and PCA transformations, was deployed in the real-time decoding pipeline. Each bit of a transmitted word was decoded independently using this pipeline. Following the decoding of all four

bits—including the appended parity bit—an even parity check was performed to validate transmission integrity. If the parity checks failed, the bit with the lowest classification confidence was toggled to correct the error, improving reliable word reconstruction.

4.3 Direct Connection

To assess the contribution of classifier complexity to decoding performance, a comparative experiment was conducted in which the SVM-based decoder was replaced with an optimal minimum error threshold classifier applied to aggregated spike counts from six output electrodes within the 0–200 ms post-stimulus window. The decision boundary was identified by exhaustively evaluating 1,000 candidate thresholds across the range of observed spike counts and selecting the one that minimized total misclassification, without making assumptions about the underlying distribution shape. Monodirectional transmission experiments were repeated under this condition, allowing direct comparison of decoding accuracy between the two classifiers.

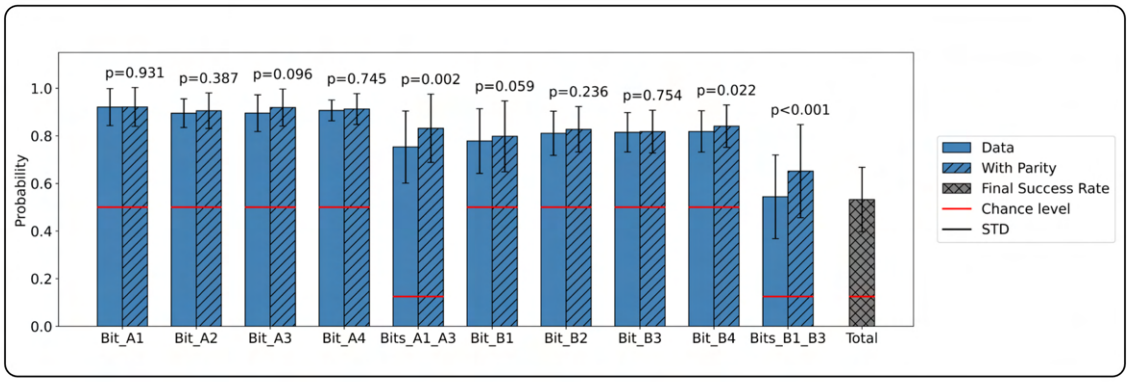

Figure 28 Machine learning-based decoding performance. Decoding accuracy for individual bits and aggregate 3-bit sequences, with and without parity-based error correction, across five independent neuronal preparations. Bits A1, A2, A3, and A4 represent the output of MEA 1; bits B1, B2, B3, and B4 represent the output of MEA 2. The rightmost bar indicates overall system performance with error correction applied. The red horizontal line indicates chance level (50% for individual bits, 12.5% for 3-bit sequences). P-values indicate the statistical significance of parity-based error correction in improving decoding accuracy.

4.4 Results

A monodirectional communication pathway was established using the setup in Figure 23 machine learning models were independently trained to decode encoded bits sequentially, one bit at a time. Given a baseline chance level of 50% per bit, decoding accuracy was evaluated against this threshold using data from five independent neuronal preparations. Results from the monodirectional testing are shown in Figure 28. Individual model performance for all four bits (three data bits plus one parity bit) is plotted separately, both with and without parity-based error correction. The final bar represents aggregate decoding accuracy for the complete 3-bit data sequence, again displayed with and without error correction against a chance level of 12.5% (1 in 8 possible 3-bit combinations). Bars indicate successful data transfer rates measured at MEA 1 output and MEA 2 output. The p-values indicate the statistical significance of parity-based error correction. The rightmost bar shows the overall system transfer rate for monodirectional communication with error correction applied.

Without error correction, the aggregated 3-bit decoding accuracy closely approximated the product of the individual bit accuracies, consistent with independent decoding errors. With parity-based correction, the aggregate success rate exceeded this product, demonstrating improved performance beyond what would be expected from independent bit decoding. This improvement results from a joint correction strategy in which the bit with the lowest classifier confidence is flipped upon detection of a parity mismatch, inducing positive dependence among bit outcomes. Accordingly,

$$P(A_1 \cap A_2 \cap A_3) = P(A_1)\,P(A_2)\,P(A_3) + \ covariance\ terms$$

where the covariance terms capture the positive correlations introduced by the parity-based correction mechanism. Because error correction creates dependencies among bits—such that correcting one bit improves the likelihood of correctly decoding others—the 3-bit sequence achieves higher overall statistical significance than would be expected from multiplying the individual bit accuracies.

Electrical stimulation is well known to drive plasticity in neural circuits by modifying synaptic efficacy, reorganizing network connectivity, and altering ensemble dynamics. Repeated stimulation was shown to induce either long-term potentiation (LTP) or long-term depression (LTD) depending on the stimulation pattern and the intrinsic state of the network, leading to strengthening or weakening of functional connections across the recorded population. These stimulation-dependent changes in connectivity have been demonstrated extensively in neural cultures and MEA-based preparations (72,73), and they significantly modified population activity patterns and evoked response structure. Because the machine-learning classifier in our system relies on spike-timing relationships and

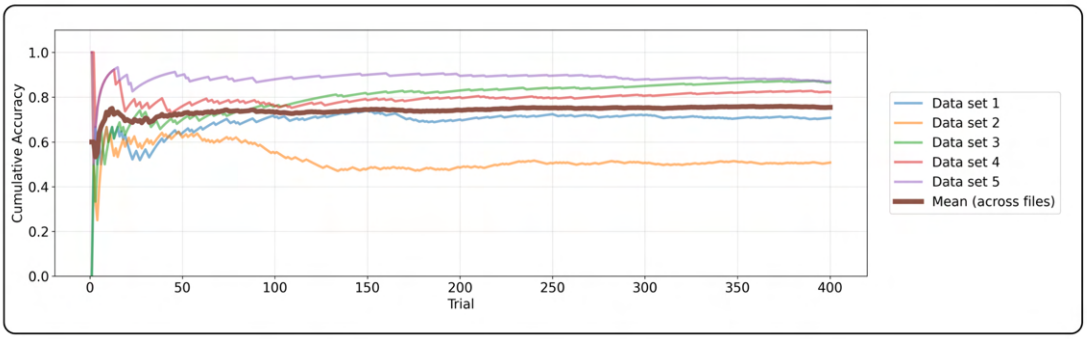

Figure 29 Temporal stability in monodirectional neural communication. Temporal stability of cumulative decoding accuracy over 400 four-bit transmissions across five independent datasets (thin colored lines) with mean performance shown as a thick dark line. Most datasets stabilize above 0.75 cumulative accuracy following an initial convergence period within the first 50 trials. Dataset 2 exhibits a sustained performance decline after approximately 100 trials, converging near chance level, while datasets 3 and 5 maintain the highest stability above 0.85 throughout the recording period. These observations suggest that periodic classifier retraining or online adaptive machine learning may be beneficial for sustaining optimal decoding performance during extended stimulation protocols.

baseline evoked response distributions, plasticity-induced reconfiguration of connectivity may degrade decoder performance over time. It is therefore essential to evaluate classifier performance longitudinally to capture these dynamics. For this reason, a quantitative analysis of decoding performance was conducted at the end of MEA 1 across five datasets to evaluate whether prolonged stimulation altered classifier accuracy. The system was tested with 400 four-bit data transmissions (corresponding to 1600 electrical stimulations), and the results are summarized in Figure 29. To capture the temporal evolution of performance, cumulative accuracy was calculated from individual trials over the 400 transmissions, providing a trajectory of overall performance as stimulation progressed. In addition, logistic regression was applied to the combined results from all five datasets to model the probability of correct classification as a smooth function of trial number.

Both analytical approaches consistently indicated that classifier performance remained stable throughout the 4000-second recording period under the applied stimulation parameters. Notably, one outlier dataset exhibited a decline in accuracy after approximately 70-word transmissions (corresponding to 280 stimulations over ~700 seconds). Minor fluctuations observed across other datasets suggest that periodic retraining of the classifier, or the incorporation of real-time (online) machine-learning adaptation, may be beneficial for sustaining optimal decoding accuracy during extended stimulation protocols.

The results from bidirectional communication experiments are shown in Figure 30. In contrast to the unidirectional transmission experiments presented in Figure 28, these bidirectional trials involved a complete round-trip communication loop in which information was transmitted from MEA 1 to MEA 2 and then returned to MEA 1, requiring sequential decoding at multiple stages. Performance is presented for the forward data path from MEA 1 to MEA 2, where A bits represent the output of MEA 1 and B bits represent the output of MEA 2, and for the return data path from MEA 2 to MEA 1, where C bits

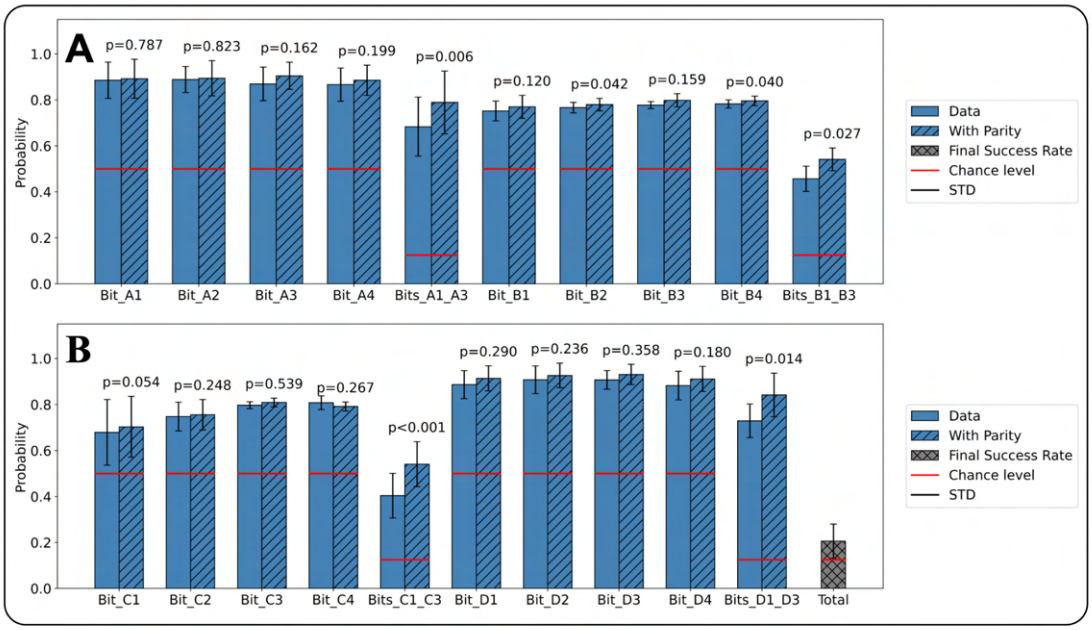

Figure 30 Bidirectional transmission performance showing bit-level and aggregate decoding accuracy across the complete communication loop, with and without parity-based error correction, reported as mean probability with standard deviation error bars. The red horizontal lines indicate chance level (0.5 for individual bits, 0.125 for 3-bit sequences). (A) Forward data path from MEA1 to MEA2. Bits A1 through A4 represent the decoded output of MEA1 and consistently exceed chance level, ranging from approximately 0.87 to 0.90. The aggregate 3-bit sequence accuracy (Bits A1-A3) improves significantly with parity correction ($p = 0.006$). Bits B1 through B4 represent the decoded output of MEA2, ranging from approximately 0.75 to 0.80, with parity correction yielding statistically significant improvements for B2 ($p = 0.042$) and B4 ($p = 0.040$). (B) Return data path from MEA2 to MEA1. Bits C1 through C4 represent the decoded output of MEA2 on the return path, ranging from approximately 0.69 to 0.81, while Bits D1 through D4 represent the final decoded output at MEA1, achieving the highest individual bit accuracy in the return path at approximately 0.88 to 0.92. The aggregate 3-bit sequence accuracy (Bits C1-C3) improves substantially with parity correction ($p < 0.001$), and the cumulative bidirectional total success rate reaches approximately 0.20, reflecting the compounded decoding challenge across the full four-stage communication loop.

represent the output of MEA 2 and D bits represent the output of MEA 1. Individual bit accuracies and aggregate 3-bit sequence accuracies are shown both with and without parity-based error correction. The final bar represents the end-to-end success rate (around 20%) for the complete bidirectional transmission, demonstrating that despite high single-bit accuracies at each stage, the multiplicative effect of individual bit errors across multiple transmission and decoding stages reduces overall system fidelity. These results highlight the critical role of error correction mechanisms in maintaining information integrity during multi-stage neural communication.

For the direct-connection condition shown in Figure 24 the decision boundary was defined using threshold-based classification on spike counts aggregated from six electrodes within the 200 ms window following stimulation. Five threshold methods were evaluated: (1) mean midpoint, calculating the arithmetic mean of each class and setting the threshold as their midpoint; (2) median midpoint, using medians instead of means for robustness to outliers; (3) optimal minimum error, which systematically tested 1,000 candidate thresholds to minimize total misclassification; (4) Fisher's Linear Discriminant, weighting by class variances; and (5) geometric mean of class means. The optimal minimum error

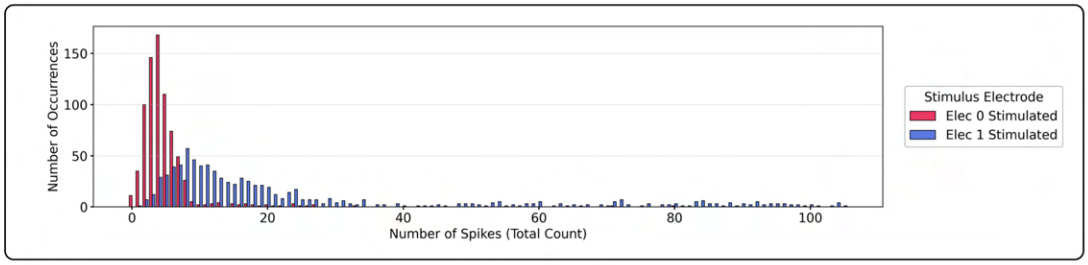

Figure 31 Distribution of total evoked spike counts across six recording electrodes within a 200 ms post-stimulus window, shown separately for stimulation at Electrode 0 (red) and Electrode 1 (blue). Both distributions are right-skewed, with the majority of stimulation events evoking fewer than 20 spikes. The substantial overlap between the two distributions in the low spike count range illustrates the fundamental limitation of single-threshold classification methods, where ambiguous evoked responses cannot be reliably attributed to a specific stimulation source based on spike count alone, motivating the use of spatiotemporal machine learning-based approaches for accurate source discrimination.

method was selected as it minimizes classification errors without assumptions about distribution shape. This approach identifies the threshold that results in the fewest misclassifications through exhaustive search. First, the minimum and maximum spike counts across both stimulus classes were identified to define the search range. Then, 1,000 candidate threshold values were generated, evenly spaced across this range. For each candidate threshold, the algorithm counted misclassification errors: Class A samples above the threshold (incorrectly classified as Class B) and Class B samples below the threshold (incorrectly classified as Class A). The threshold producing the minimum total error was selected as the optimal decision boundary

As illustrated in Figure 31, the distributions for the two stimulation sources partially overlapped in several trials, limiting the separability achievable with simple thresholding.

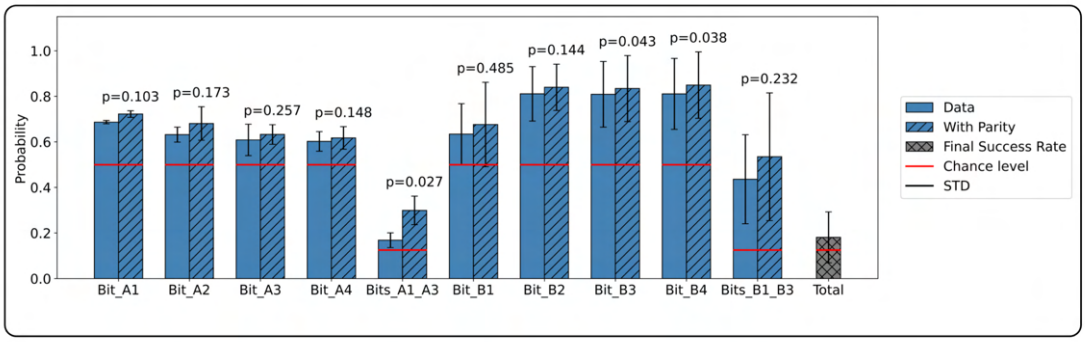

Figure 32 Decoding accuracy comparison between threshold-based and machine learning-based classification in a hybrid monodirectional pipeline, with and without parity-based error correction, reported as mean probability with standard deviation error bars. The red horizontal lines indicate chance level (0.5 for individual bits, 0.125 for 3-bit sequences). Bits A1 through A4 represent the threshold-based decoded output of MEA1, achieving individual bit accuracies between approximately 0.60 and 0.69, only marginally above chance level, with parity correction yielding no statistically significant improvement across any A-bit channel. The aggregate 3-bit sequence accuracy (Bits A1-A3) improves with parity correction ($p = 0.027$) but remains near chance level at approximately 0.15 to 0.29. In contrast, Bits B1 through B4, decoded using machine learning classification at MEA2, achieve substantially higher individual bit accuracies between approximately 0.63 and 0.84, with statistically significant parity improvements observed for B3 ($p = 0.043$) and B4 ($p = 0.038$). The overall final success rate of approximately 0.18 reflects the compounded limitation introduced by the threshold-based first stage, demonstrating the insufficiency of threshold-based approaches for reliable neural communication in multi-MEA systems and reinforcing the necessity of machine learning-based decoding across all stages of the pipeline.

Overall, this approach yielded bit-level accuracies of approximately 60%, which is only marginally above chance level (50%) (shown on Figure 32). For bidirectional transmission, the accuracy of this method proved insufficient for reliable transmission of three-bit messages, as performance approached or fell below chance expectations. These results were consistent across both mono-directional and bidirectional experiments and highlight the limitations of threshold-based decoding. In contrast, they underscore the added value of the proposed machine-learning-based classifier in improving transmission stability and robustness across neural cultures.

5 DISCUSSION

5.1 Summary of Demonstrated Findings

This study demonstrates the Virtual White Matter (VWM), a complete closed-loop platform capable of establishing real-time functional connectivity between biologically independent neural cultures maintained in physically separate multi-electrode array (MEA) dishes. Across two research aims, the system was shown to (1) reliably detect spontaneous action potentials in a source culture and trigger precisely timed electrical stimulation in a target culture with a fixed 200 ms delay; (2) evoke discriminable, spatially distinct post-stimulus activity patterns that could be classified by machine learning algorithms; (3) support bidirectional communication between two cultures in a closed-loop configuration; and (4) encode, transmit, and decode structured three-bit binary messages across separate biological neural networks using real-time Support Vector Machine classification combined with parity-based error correction. These results, validated across five independent neural preparations and over 1,600 stimulations per longitudinal dataset, establish VWM as a technically viable and biologically grounded platform for inter-network neural communication.

The biological validity of all recorded signals was confirmed using MK-801, an NMDA receptor antagonist. Suppression of spontaneous activity in the source dish eliminated stimulation events in the target dish, while direct application of MK-801 to the target dish abolished stimulus-evoked responses without affecting stimulation artifacts. Recovery of activity following washout confirmed that the observed neural responses were genuinely biological rather than artifactual. These controls are a necessary foundation for interpreting all subsequent classification and transmission results.

5.2 Spike Detection and Artifact Rejection

A key technical contribution of this work is the double-threshold, multi-criterion spike detection algorithm developed specifically for the signal characteristics of dissociated rat cortical cultures on MED64 MEAs. Conventional single-threshold approaches detect voltage excursions above a fixed amplitude, making them susceptible to stimulation artifacts, which share temporal and morphological overlap with genuine action potentials. The double-threshold method requires a signal to cross a negative threshold, subsequently cross a positive threshold within defined timing bounds, and then cross zero within a constrained window, while remaining below a noise ceiling in the milliseconds surrounding the event. This combination of amplitude, timing, and morphological constraints effectively discriminates biological spikes from artifacts.

The importance of this distinction was empirically demonstrated: when single-threshold detection was used on recordings from MK-801-treated dishes, in which no biological activity was present, machine learning classifiers still achieved above-chance accuracy, indicating that stimulation artifacts were being detected and inadvertently used as classification features. With double-threshold detection under the same conditions, classifier accuracy dropped to chance level, confirming that artifact contamination was eliminated. All subsequent analyses in Aim 1 and Aim 2 were therefore conducted exclusively using the double-threshold method. This finding has broad implications for any closed-loop MEA system in which stimulation and recording occur simultaneously: artifact rejection is not merely a signal-quality concern but a scientific validity concern, because artifact-driven classification can produce falsely optimistic performance metrics that do not reflect genuine neural information transfer.

5.3 Classification, Temporal Features, and Information Encoding

In Aim 1, machine learning classification of post-stimulus evoked responses demonstrated that distinct, decodable activity patterns could be reliably elicited by stimulating two spatially separated target electrodes. Feature importance analysis using information gain, chi-square tests, and Fisher's score consistently identified the first 10 ms of the post-stimulus window as the most informative period for classification. This finding has a straightforward biological interpretation: within the first 10 ms, the initial propagation of electrically evoked activity reaches nearby electrodes before the network enters a generalized burst state. During bursting, a large proportion of neurons fire synchronously regardless of stimulation source, effectively destroying spatial specificity. Extending the classification window beyond 10 ms therefore degrades performance by diluting early, location-specific signals with burst-related activity that is common to both stimulation conditions. This result has a direct implication for system design: real-time decoding latency can be minimized to 10 ms post-stimulus without sacrificing accuracy, which is considerably shorter than the 200 ms analysis window used for initial exploration.

The choice of classifier mattered substantially. In Aim 2, Support Vector Machine classifiers with a sigmoid kernel (C = 10) consistently outperformed both K-Nearest Neighbors and Random Forest classifiers across all five preparations, and all three machine learning methods substantially outperformed threshold-based spike counting. The threshold approach, which compared total spike counts from six output electrodes within the 200 ms post-stimulus window, yielded bit-level accuracies of approximately 60%, only marginally above the 50% chance level, and produced word-level transmission rates near chance for three-bit sequences. This poor performance reflects a fundamental limitation:

the spike count distributions evoked by the two stimulation electrodes partially overlapped, and a single scalar threshold cannot resolve this ambiguity. In contrast, the SVM classifier operated on 1 ms-binned spike trains across six electrodes, constructing a 200-dimensional feature space per electrode (1,200 features in total) that captured subtle spatiotemporal differences in response patterns invisible to scalar thresholding. The combination of z-score normalization, which removed electrode-level amplitude biases attributable to impedance variability and tissue coupling differences, and PCA-based dimensionality reduction, which retained 95% of variance while suppressing unstructured noise, allowed the SVM to identify consistent decision boundaries across preparations despite substantial culture-to-culture variability.

The selection of SVM over deep learning approaches was deliberate and practically motivated. The number of stimulations available for training in each session (400–800) is insufficient to support deep neural network training without overfitting, given the high-dimensional feature space relative to sample size. SVMs, by contrast, are well-suited to limited training data sizes while still providing nonlinear decision boundaries through kernel mapping. Among classifiers tested, the sigmoid kernel outperformed other linear models.

5.4 Structured Binary Communication and Error Correction

Aim 2 extended VWM from a signal-relay system to a structured information-transfer system. Three-bit binary words, augmented with a parity bit to form four-bit transmission packets, were encoded as spatiotemporal stimulation sequences delivered to the input electrodes of MEA 1. The resulting evoked responses were decoded in real time by the SVM classifier, and the corrected word was re-encoded and transmitted to MEA 2, where

a second SVM model decoded the response. In the bidirectional configuration, the decoded output of MEA 2 was further re-encoded and transmitted back to MEA 1, completing a full round-trip communication loop.

Parity-based error correction improved aggregate transmission accuracy in a statistically significant and mechanistically interpretable way. Without correction, the probability of correctly transmitting a three-bit word approximated the product of the individual bit accuracies, consistent with independent decoding errors across bits. With parity correction, this aggregate rate was exceeded because the confidence-based bit-toggling strategy introduced positive statistical dependence among bit outcomes: when the classifier's least confident bit is toggled upon a parity failure, the correction simultaneously increases the probability that all three data bits are correct. This joint correction benefit explains why the improvement in aggregate word accuracy was statistically more significant than could be expected from simple multiplication of individual bit improvements.

The current parity scheme is limited to detecting and correcting single-bit errors. In sessions where decoding accuracy was lower, multi-bit errors may have occurred, leading to erroneous corrections in which the wrong bit was toggled. Future implementations should consider stronger error-correcting codes, such as Hamming(7,4) codes, which can correct any single-bit error and detect two-bit errors within a seven-bit codeword, or Reed-Solomon codes for burst-error environments. Implementing these schemes requires no hardware changes; they operate entirely in the classification and encoding software layer. The practical cost is a reduction in information bandwidth, as more bits must be allocated to redundancy rather than data, but this trade-off is well justified given the inherent stochasticity of biological neural responses.

The end-to-end success rate of approximately 20% for complete bidirectional transmission reflects a fundamental mathematical reality of multi-stage communication systems: errors compound across stages. If each of the four decoding stages (MEA 1 output A, MEA 2 output B, MEA 2 output C, MEA 1 output D) achieves a word-level accuracy of approximately 70%, the probability of a correct end-to-end transmission is approximately $0.70^4 \approx 0.24$. Improving individual-stage accuracy has a multiplicative effect on end-to-end fidelity, underscoring that advances in decoder robustness will disproportionately benefit multi-stage communication chains. Alternatively, staging error correction at each node rather than only at the terminal node could intercept and correct errors before they propagate to subsequent stages.

5.5 Temporal Stability and Plasticity Considerations

A critical concern for any biocomputing platform based on electrical stimulation is whether repeated stimulation induces plasticity changes that degrade decoder performance over time. Electrical stimulation is well established to modify synaptic efficacy and network connectivity through mechanisms including long-term potentiation (LTP) and long-term depression (LTD), with the direction and magnitude of plasticity depending on stimulation frequency, pattern, and the intrinsic state of the network. Because the SVM classifier in VWM is trained on baseline evoked response distributions, any plasticity-driven shift in those distributions will cause a mismatch between the trained model and the current network state, progressively degrading accuracy.

The longitudinal analysis conducted across 400 four-bit word transmissions (1,600 stimulations, approximately 4,000 seconds) demonstrated that classifier performance remained stable in four of five datasets under the applied stimulation parameters. This

stability suggests that the chosen protocol, biphasic charge-balanced pulses at 10 μA amplitude with 1-second inter-bit and 2-second inter-word intervals, operates within a stimulation regime that does not drive strong or net-directional plasticity. The charge density of 2×10^{-4} C/cm² per phase falls within published safe limits for platinum electrodes, and the temporal spacing between stimulations may allow synaptic recovery before the next event, limiting Hebbian reinforcement. One outlier dataset exhibited a monotonic accuracy decline beginning after approximately 280 stimulations, suggesting that culture-specific factors, such as electrode-neuron coupling stability, initial synaptic connectivity state, or spontaneous network drift, can produce plasticity profiles that fall outside the range captured by the other preparations. This heterogeneity highlights the need for online adaptive strategies in extended experiments.

The present study intentionally used a fixed, pre-trained classifier to isolate and quantify the intrinsic stability limits of the communication protocol. Future implementations should incorporate online learning algorithms that continuously update classifier parameters using recent stimulation trials or implement periodic recalibration sessions in which a short calibration sequence is used to retrain the decoder to current network conditions. Both strategies have precedent in brain-computer interface literature for managing electrode impedance drift and neuronal ensemble changes over time. An additional approach would involve designing stimulation protocols that actively counterbalance plasticity, for example, by alternating between LTP-promoting and LTD-promoting patterns to maintain a stable net synaptic state across the recorded population.

5.6 Broader Implications and Future Directions

VWM addresses a structural gap in in-vitro neuroscience: the inability to model interregional brain dynamics using isolated single-dish preparations. Biological neural networks are characterized by reciprocal long-range connectivity between functionally distinct regions, and many of the most important emergent properties of brain function, including sensory integration, working memory, and executive control, arise from the dynamics of this interregional communication rather than from any single region in isolation. VWM provides a scalable, hardware framework for recreating such dynamics *in vitro*, with the additional advantage that each component network can be independently characterized, pharmacologically manipulated, or genetically modified. For example, a dish containing hippocampal neurons could be bidirectionally linked to a dish containing neurons carrying a mutation associated with Alzheimer's disease, enabling direct study of how pathological network dynamics in one region propagate and distort activity in a connected healthy region.

For biocomputing applications, VWM provides a concrete implementation path for networked biological computation in which multiple neural cultures exchange structured information and collaborate on tasks that exceed the representational capacity of any single isolated preparation. The successful demonstration of structured binary communication validates the core premise that spatiotemporal stimulation patterns can encode symbolic information in a biological medium that is decodable at a remote biological site. Scaling this architecture requires addressing several technical constraints discussed below, but the fundamental feasibility is now established.

The current binary encoding scheme, which uses electrode identity (which of two electrodes is stimulated) to represent each bit, provides a measured information bandwidth of approximately 0.375 bits per second, calculated from 3 data bits per word transmitted at a rate of one word per 5 seconds. This bandwidth is severely constrained by the inter-bit and inter-word timing requirements imposed by burst recovery dynamics. Meaningful bandwidth improvements require further studies. The choice of using single pulses and two electrodes per bit represents only one instance of a substantially broader design space for neural encoding. Rather than relying solely on spatial binary codes (i.e., which electrode is stimulated) information can be conveyed through richer stimulation parameters including pulse amplitude, width, inter-pulse intervals, burst structures, or systematic parameter sweeps. Such approaches enable multi-level or continuous-valued encoding, removing the constraint of strictly binary representation.

Neural systems are inherently sensitive to spatiotemporal structure beyond stimulation location alone. Variations in temporal patterning, such as burst timing, phase relationships, or non-periodic pulse trains, can evoke distinct network responses even when delivered through the same electrode pair, enabling information encoding in the temporal domain wherein different stimulus patterns represent different symbols without increasing electrode count. Furthermore, biomimetic encoding strategies that mimic physiological firing statistics have shown improved interpretability in both central and peripheral nervous systems. Multi-site spatiotemporal strategies, such as coordinated stimulation across multiple electrodes with varying relative timing, can induce qualitatively different network states, supporting non-binary, state-dependent encoding mechanisms. Collectively, pulse shape, timing, sequence structure, and adaptive closed-loop policies represent additional

encoding dimensions that could enable higher-capacity, more biologically compatible neural communication channels beyond the binary electrode-based scheme demonstrated here.

5.7 Limitations

Several limitations constrain the current system. First, operating system-level timing non-determinism in the PC-based acquisition and processing pipeline introduces variable latencies in the spike detection-to-stimulation loop. The ARM microcontroller circular buffer mitigates the worst effects, but true deterministic real-time performance would require a dedicated embedded platform such as a field-programmable gate array (FPGA) with hardware spike detection, eliminating operating system overhead entirely. This transition would also reduce power consumption and enable compact packaging necessary for incubator-compatible deployment.

Second, culture-to-culture variability remains a substantial challenge. Each preparation requires individualized electrode selection, parameter optimization, and classifier training, preventing any single trained model from being deployed across preparations without recalibration. Addressing this variability may ultimately require advances in culture standardization, including controlled cell-type composition, micropatterned network architectures that impose reproducible connectivity, or clonal cell lines with reduced stochastic genetic variation, rather than purely algorithmic solutions.

Third, the limited lifespan of dissociated cortical cultures, approximately 48 days post-plating, with meaningful activity typically between days 14 and 48, constrains the duration of any single experimental series. This lifespan limitation may be less restrictive in VWM assemblies of multiple linked preparations, where individual deteriorating cultures can in

principle be replaced while the connected network preserves global communication structure. Organoid-based preparations may offer longer lifespans and more stable network dynamics but introduce new challenges for electrode access, stimulation uniformity, and signal-to-noise ratios in three-dimensional tissue.

Fourth, the machine learning pipeline requires between 400 and 800 stimulations for initial training and may require periodic retraining to compensate for network drift. This training cost represents a significant fraction of the viable experimental window for a given preparation. Online learning approaches that update classifier parameters continuously from incoming stimulation data, without requiring a discrete offline training phase, would substantially reduce this overhead and improve adaptability to gradual network changes.

6 CONCLUSION

This dissertation presents Virtual White Matter (VWM), the first system to enable real-time functional digital connectivity between biologically independent neural cultures in physically separate MEA dishes. By detecting action potentials in a source culture and triggering precisely timed electrical stimulation in a target culture, VWM recreates the inter-regional communication dynamics that define the functional organization of the brain *in vivo*, while operating entirely within the tractable and manipulable context of *in vitro* preparations.

Aim 1 established the core VWM platform and validated its biological integrity through MK-801 pharmacological controls, confirmed the consistency of stimulus-to-response delays, and demonstrated that machine learning classifiers can decide which of two target electrodes was stimulated from the resulting evoked activity. A novel double-threshold spike detection algorithm was developed and shown to be essential for eliminating stimulation artifacts from the classification feature set, a finding with direct relevance to any closed-loop MEA system in which simultaneous stimulation and recording are performed. Bidirectional communication was demonstrated, and the emergent feedback dynamics observed in the unconstrained bidirectional configuration provide empirical data on positive feedback loop formation in coupled biological networks.

Aim 2 extended VWM to structured symbolic communication, demonstrating that three-bit binary messages can be encoded into spatiotemporal stimulation sequences, transmitted through biological neural tissue, and decoded in real time with above-chance accuracy at each stage of a multi-hop communication chain. Parity-based error correction with confidence-weighted bit toggling improved word-level transmission accuracy with

statistical significance across five independent neural preparations. Longitudinal analysis over 1,600 stimulations confirmed that the stimulation protocol did not induce significant plasticity-driven decoder degradation in most preparations, establishing a viable operating regime for extended biocomputing experiments. The superiority of SVM-based decoding over threshold-based spike counting was quantified, demonstrating that spatiotemporal feature representations are necessary for reliable multi-bit neural communication, simple scalar metrics are insufficient.

Together, these results resolve the fundamental feasibility question that motivated this work: physically separated biological neural networks can exchange structured symbolic information through an engineered digital communication channel. This demonstration constitutes a proof of concept for distributed biocomputing architectures in which multiple biological processing units contribute to computation through structured inter-network communication rather than in isolation. The VWM platform is hardware-agnostic with respect to specimen type, scalable to more than two linked cultures, and compatible with *in vivo* preparations, making it a flexible foundation for a broad range of future applications.

Significant challenges remain before VWM can be deployed as a robust biocomputing or therapeutic tool. Bandwidth is constrained by the inter-stimulus timing requirements of post-burst recovery; culture variability necessitates individualized calibration; the limited lifespan of dissociated cultures restricts experimental duration; and hardware non-determinism in the current PC-based implementation limits timing precision. Each of these challenges has identified technical solutions, richer encoding schemes, standardized culture protocols, organoid-based preparations, and FPGA-based processing, and the

principles demonstrated here provide a concrete roadmap for addressing them systematically.

Beyond the specific results reported here, VWM opens conceptual territory that has not been experimentally accessible with previous tools. The ability to link heterogeneous neural populations from different species, brain regions, genetic backgrounds, or developmental stages in controlled bidirectional communication creates a new class of experimental model for studying interregional plasticity, pathological network propagation, and the computational properties of biological tissue. As the field advances toward increasingly complex assemblies of linked neural preparations, the methods, validations, and design principles established in this dissertation provide the technical and scientific foundation upon which those systems can be built.

7 REFERENCES

1. Napoli A, Obeid I. Investigating brain functional evolution and plasticity using microelectrode array technology. Brain Research Bulletin. 2015;119:127–35. doi:10.1016/j.brainresbull.2015.10.002 PubMed PMID: 26476356.

2. Massobrio P, Tessadori J, Chiappalone M, Ghirardi M. In vitro studies of neuronal networks and synaptic plasticity in invertebrates and in mammals using multielectrode arrays. Neural Plast. 2015;2015:196195. doi:10.1155/2015/196195 PubMed PMID: 25866681; PubMed Central PMCID: PMC4381683.

3. Napoli A, Xie J, Obeid I. Understanding the temporal evolution of neuronal connectivity in cultured networks using statistical analysis. BMC Neuroscience. 2014 Jan;15(1):17. doi:10.1186/1471-2202-15-17 PubMed PMID: 24443925.

4. Kagan BJ, Kitchen AC, Tran NT, Habibollahi F, Khajehnejad M, Parker BJ, et al. In vitro neurons learn and exhibit sentience when embodied in a simulated game-world. Neuron. 2022 Dec 7;110(23):3952-3969.e8. doi:10.1016/j.neuron.2022.09.001 PubMed PMID: 36228614; PubMed Central PMCID: PMC9747182.

5. Bisio M, Pimashkin A, Buccelli S, Tessadori J, Semprini M, Levi T, et al. Closed-Loop Systems and In Vitro Neuronal Cultures: Overview and Applications. In: Chiappalone M, Pasquale V, Frega M, editors. In Vitro Neuronal Networks: From Culturing Methods to Neuro-Technological Applications [Internet]. Cham: Springer International Publishing; 2019 [cited 2024 Aug 28]. p. 351–87. Available from: https://doi.org/10.1007/978-3-030-11135-9_15 doi:10.1007/978-3-030-11135-9_15

6. Eytan D, Brenner N, Marom S. Selective adaptation in networks of cortical neurons. J Neurosci. 2003 Oct 15;23(28):9349–56. doi:10.1523/JNEUROSCI.23-28-09349.2003 PubMed PMID: 14561862; PubMed Central PMCID: PMC6740578.

7. le Feber J, Stegenga J, Rutten WLC. The effect of slow electrical stimuli to achieve learning in cultured networks of rat cortical neurons. PLoS One. 2010 Jan 25;5(1):e8871. doi:10.1371/journal.pone.0008871 PubMed PMID: 20111726; PubMed Central PMCID: PMC2810341.

8. Shahaf G, Marom S. Learning in networks of cortical neurons. J Neurosci. 2001 Nov 15;21(22):8782–8. doi:10.1523/JNEUROSCI.21-22-08782.2001 PubMed PMID: 11698590; PubMed Central PMCID: PMC6762268.

9. DeMarse TB, Wagenaar DA, Blau AW, Potter SM. The Neurally Controlled Animat: Biological Brains Acting with Simulated Bodies. Autonomous Robots. 2001 Nov 1;11(3):305–10. doi:10.1023/A:1012407611130

10. Ruaro ME, Bonifazi P, Torre V. Toward the neurocomputer: image processing and pattern recognition with neuronal cultures. IEEE Trans Biomed Eng. 2005 Mar;52(3):371–83. doi:10.1109/TBME.2004.842975 PubMed PMID: 15759567.

11. Feinerman O, Rotem A, Moses E. Reliable neuronal logic devices from patterned hippocampal cultures. Nature Phys. 2008 Dec;4(12):967–73. doi:10.1038/nphys1099

12. Bakkum DJ, Chao ZC, Potter SM. Spatio-temporal electrical stimuli shape behavior of an embodied cortical network in a goal-directed learning task. J Neural Eng. 2008 Aug;5(3):310. doi:10.1088/1741-2560/5/3/004

13. Novellino A, D'Angelo P, Cozzi L, Chiappalone M, Sanguineti V, Martinoia S. Connecting Neurons to a Mobile Robot: An In Vitro Bidirectional Neural Interface. Comput Intell Neurosci. 2007;2007:12725. doi:10.1155/2007/12725 PubMed PMID: 18350128; PubMed Central PMCID: PMC2266971.

14. Warwick K, Xydas D, Nasuto S, Becerra V, Hammond M, Downes J, et al. Controlling a Mobile Robot with a Biological Brain. Defence Science Journal. 2010 Jan 30;60:5–14. doi:10.14429/dsj.60.11

15. Reger BD, Fleming KM, Sanguineti V, Alford S, Mussa-Ivaldi FA. Connecting brains to robots: an artificial body for studying the computational properties of neural tissues. Artif Life. 2000;6(4):307–24. doi:10.1162/106454600300103656 PubMed PMID: 11348584.

16. DeMarse TB, Dockendorf KP. Adaptive flight control with living neuronal networks on microelectrode arrays. In: Proceedings. 2005 IEEE International Joint Conference on Neural Networks, 2005. [Internet]. Montreal, QC, Canada: IEEE; 2005 [cited 2024 Aug 28]. p. 1548–51. Available from: http://ieeexplore.ieee.org/document/1556108/ doi:10.1109/IJCNN.2005.1556108

17. Cai H, Ao Z, Tian C, Wu Z, Liu H, Tchieu J, et al. Brain organoid reservoir computing for artificial intelligence. Nat Electron. 2023 Dec;6(12):1032–9. doi:10.1038/s41928-023-01069-w

18. Sumi T, Yamamoto H, Katori Y, Moriya S, Konno T, Sato S, et al. Biological neurons act as generalization filters in reservoir computing. Proc Natl Acad Sci USA. 2023 Jun 20;120(25):e2217008120. doi:10.1073/pnas.2217008120

19. Berger TW, Ahuja A, Courellis SH, Deadwyler SA, Erinjippurath G, Gerhardt GA, et al. Restoring lost cognitive function. IEEE Eng Med Biol Mag. 2005;24(5):30–44. doi:10.1109/memb.2005.1511498 PubMed PMID: 16248115.

20. DeMare L. Wetware: A Computer in Every Living Cell. Yale J Biol Med. 2011 Jun;84(2):174–5. PubMed PMID: null; PubMed Central PMCID: PMC3117417.

21. Jordan FD, Kutter M, Comby JM, Brozzi F, Kurtys E. Open and remotely accessible Neuroplatform for research in wetware computing. Front Artif Intell. 2024 May 2;7:1376042. doi:10.3389/frai.2024.1376042 PubMed PMID: 38756757; PubMed Central PMCID: PMC11097343.

22. Smirnova L. Biocomputing with organoid intelligence. Nat Rev Bioeng. 2024 Aug;2(8):633–4. doi:10.1038/s44222-024-00200-6

23. Smirnova L, Caffo BS, Gracias DH, Huang Q, Morales Pantoja IE, Tang B, et al. Organoid intelligence (OI): the new frontier in biocomputing and intelligence-in-a-dish. Front Sci. 2023 Feb 28;1. doi:10.3389/fsci.2023.1017235

24. Goñi-Moreno A, Nikel PI. High-Performance Biocomputing in Synthetic Biology–Integrated Transcriptional and Metabolic Circuits. Front Bioeng Biotechnol. 2019 Mar 11;7. doi:10.3389/fbioe.2019.00040

25. Vallejo-Mancero B, Faci-Lázaro S, Zapata M, Soriano J, Madrenas J. Real-time hardware emulation of neural cultures: A comparative study of in vitro, in silico and in duris silico models. Neural Networks. 2024 Nov 1;179:106593. doi:10.1016/j.neunet.2024.106593

26. Mariana M, Roque C, Baltazar G, Cairrao E. In Vitro Model for Ischemic Stroke: Functional Analysis of Vascular Smooth Muscle Cells. Cell Mol Neurobiol. 2022 Oct 1;42(7):2289–304. doi:10.1007/s10571-021-01103-5

27. Van Breedam E, Ponsaerts P. Promising Strategies for the Development of Advanced In Vitro Models with High Predictive Power in Ischaemic Stroke Research. International Journal of Molecular Sciences. 2022 Jan;23(13):13. doi:10.3390/ijms23137140

28. Chiappalone M, Cota VR, Carè M, Di Florio M, Beaubois R, Buccelli S, et al. Neuromorphic-Based Neuroprostheses for Brain Rewiring: State-of-the-Art and Perspectives in Neuroengineering. Brain Sci. 2022 Nov 19;12(11):1578. doi:10.3390/brainsci12111578 PubMed PMID: 36421904; PubMed Central PMCID: PMC9688667.

29. Shupe LE, Miles FP, Jones G, Yun R, Mishler J, Rembado I, et al. Neurochip3: An Autonomous Multichannel Bidirectional Brain-Computer Interface for Closed-Loop Activity-Dependent Stimulation. Front Neurosci. 2021 Aug 19;15. doi:10.3389/fnins.2021.718465

30. Henley C. The Neuron [Internet]. 2021 Jan 1 [cited 2026 Apr 8]. Available from: https://openbooks.lib.msu.edu/neuroscience/chapter/the-neuron/

31. Urone PP, Hinrichs R, Beceiro-Novo S. Nerve Conduction–Electrocardiograms [Internet]. 2012 Jan 23 [cited 2026 Apr 8]. Available from: https://openbooks.lib.msu.edu/collegephysics/chapter/nerve-conduction-electrocardiograms/

32. Cannon SC. Pathomechanisms in channelopathies of skeletal muscle and brain. Annu Rev Neurosci. 2006;29:387–415. doi:10.1146/annurev.neuro.29.051605.112815 PubMed PMID: 16776591.

33. Kullmann DM, Waxman SG. Neurological channelopathies: new insights into disease mechanisms and ion channel function. J Physiol. 2010 Jun 1;588(Pt 11):1823–7. doi:10.1113/jphysiol.2010.190652 PubMed PMID: 20375141; PubMed Central PMCID: PMC2901970.

34. Yizhar O, Fenno LE, Prigge M, Schneider F, Davidson TJ, O'Shea DJ, et al. Neocortical excitation/inhibition balance in information processing and social dysfunction. Nature. 2011 Sep;477(7363):171–8. doi:10.1038/nature10360

35. Cui H, Xie X, Xu S, Chan LLH, Hu Y. Electrochemical characteristics of microelectrode designed for electrical stimulation. BioMedical Engineering OnLine. 2019 Aug 1;18(1):86. doi:10.1186/s12938-019-0704-8

36. Holt GR, Koch C. Electrical Interactions via the Extracellular Potential Near Cell Bodies. J Comput Neurosci. 1999 Mar 1;6(2):169–84. doi:10.1023/A:1008832702585

37. Quiroga RQ, Nadasdy Z, Ben-Shaul Y. Unsupervised spike detection and sorting with wavelets and superparamagnetic clustering. Neural Comput. 2004 Aug;16(8):1661–87. doi:10.1162/089976604774201631 PubMed PMID: 15228749.

38. Lewicki MS. A review of methods for spike sorting: the detection and classification of neural action potentials. Network: Computation in Neural Systems. 1998 Jan;9(4):R53–78. doi:10.1088/0954-898X_9_4_001

39. Erofeev A, Antifeev I, Bolshakova A, Bezprozvanny I, Vlasova O. In Vivo Penetrating Microelectrodes for Brain Electrophysiology. Sensors (Basel). 2022 Nov 23;22(23):9085. doi:10.3390/s22239085 PubMed PMID: 36501805; PubMed Central PMCID: PMC9735502.

40. Utah Array, Electrodes | Products. Blackrock Neurotech [Internet]. [cited 2025 Mar 5]. Available from: https://blackrockneurotech.com/products/utah-array/

41. Marr D. MED Probe for Basic / Plex System. med64.com [Internet]. [cited 2025 Mar 5]. Available from: https://www.med64.com/products/med-probe-mea/med-probe-basic-plex/

42. High-Density Microelectrode Array (HD-MEA) | 3Brain [Internet]. [cited 2025 Mar 5]. Available from: https://www.3brain.com/

43. Single-well HD-MEA Platform | BioCAM DupleX | 3Brain [Internet]. [cited 2025 Mar 5]. Available from: https://www.3brain.com/products/single-well/biocam-duplex

44. SiNAPS Pixel Probes - NeuroNexus [Internet]. [cited 2026 Apr 8]. Available from: https://www.neuronexus.com/products/electrode-arrays/sinaps/

45. Neuropixels NEW [Internet]. [cited 2025 Mar 5]. Home | Neuropixels. Available from: https://www.neuropixels.org

46. CerePort Plug, Standalone, Adaptors & Accessories | Products. Blackrock Neurotech [Internet]. [cited 2025 Mar 6]. Available from: https://blackrockneurotech.com/products/cereport-plug-standalone/

47. Flesher SN, Downey JE, Weiss JM, Hughes CL, Herrera AJ, Tyler-Kabara EC, et al. A brain-computer interface that evokes tactile sensations improves robotic arm control. Science. 2021 May 21;372(6544):831–6. doi:10.1126/science.abd0380 PubMed PMID: 34016775; PubMed Central PMCID: PMC8715714.

48. Hochberg LR, Serruya MD, Friehs GM, Mukand JA, Saleh M, Caplan AH, et al. Neuronal ensemble control of prosthetic devices by a human with tetraplegia. Nature. 2006 Jul;442(7099):164–71. doi:10.1038/nature04970

49. Davis TS, Wark H a. C, Hutchinson DT, Warren DJ, O'Neill K, Scheinblum T, et al. Restoring motor control and sensory feedback in people with upper extremity amputations using arrays of 96 microelectrodes implanted in the median and ulnar nerves. J Neural Eng. 2016 Jun;13(3):036001. doi:10.1088/1741-2560/13/3/036001 PubMed PMID: 27001946.

50. Wilson GH, Stavisky SD, Willett FR, Avansino DT, Kelemen JN, Hochberg LR, et al. Decoding spoken English from intracortical electrode arrays in dorsal precentral gyrus.

J Neural Eng. 2020 Nov 25;17(6):066007. doi:10.1088/1741-2552/abbfef PubMed PMID: 33236720; PubMed Central PMCID: PMC8293867.

51. Willett FR, Avansino DT, Hochberg LR, Henderson JM, Shenoy KV. High-performance brain-to-text communication via handwriting. Nature. 2021 May;593(7858):249–54. doi:10.1038/s41586-021-03506-2

52. Hughes CL, Flesher SN, Weiss JM, Downey JE, Boninger M, Collinger JL, et al. Neural stimulation and recording performance in human sensorimotor cortex over 1500 days. J Neural Eng. 2021 Aug 13;18(4). doi:10.1088/1741-2552/ac18ad PubMed PMID: 34320481; PubMed Central PMCID: PMC8500669.

53. Magnusson Fredlund J. Literature Study on the Technical Development of Invasive Recording Brain Computer Interfaces. Proceedings of Clinical Innovations [Internet]. 2024 [cited 2025 Mar 14]. Available from: http://lup.lub.lu.se/student-papers/record/9158403

54. Du ZJ, Kolarcik CL, Kozai TDY, Luebben SD, Sapp SA, Zheng XS, et al. Ultrasoft microwire neural electrodes improve chronic tissue integration. Acta Biomaterialia. 2017 Apr 15;53:46–58. doi:10.1016/j.actbio.2017.02.010

55. Weltman A, Yoo J, Meng E. Flexible, Penetrating Brain Probes Enabled by Advances in Polymer Microfabrication. Micromachines. 2016 Oct;7(10):10. doi:10.3390/mi7100180

56. Yamashita K, Sawahata H, Yamagiwa S, Numano R, Koida K, Kawano T. Floating 5-μm-Diameter Needle for Low Invasive Chronic Recording. In: 2019 20th International

Conference on Solid-State Sensors, Actuators and Microsystems & Eurosensors XXXIII (TRANSDUCERS & EUROSENSORS XXXIII) [Internet]. 2019 [cited 2025 Mar 6]. p. 302–5. Available from: https://ieeexplore.ieee.org/abstract/document/8808218 doi:10.1109/TRANSDUCERS.2019.8808218

57. Mestais CS, Charvet G, Sauter-Starace F, Foerster M, Ratel D, Benabid AL. WIMAGINE: wireless 64-channel ECoG recording implant for long term clinical applications. IEEE Trans Neural Syst Rehabil Eng. 2015 Jan;23(1):10–21. doi:10.1109/TNSRE.2014.2333541 PubMed PMID: 25014960.

58. Precision [Internet]. [cited 2026 Apr 8]. Available from: https://precisionneuro-io-2025-92sd.vercel.app

59. Musk E. An Integrated Brain-Machine Interface Platform With Thousands of Channels. J Med Internet Res. 2019 Oct 31;21(10):e16194. doi:10.2196/16194 PubMed PMID: 31642810; PubMed Central PMCID: PMC6914248.

60. Hanson TL, Diaz-Botia CA, Kharazia V, Maharbiz MM, Sabes PN. The “sewing machine” for minimally invasive neural recording [Internet]. bioRxiv; 2019 [cited 2025 Mar 6]. p. 578542. Available from: https://www.biorxiv.org/content/10.1101/578542v1 doi:10.1101/578542

61. Shadmani A, Viswam V, Chen Y, Bounik R, Dragas J, Radivojevic M, et al. Stimulation and Artifact-suppression Techniques for in-vitro High-density Microelectrode Array Systems. IEEE Trans Biomed Eng. 2019 Sep;66(9):2481–90.

doi:10.1109/TBME.2018.2890530 PubMed PMID: 30605090; PubMed Central PMCID: PMC6711758.

62. Ross, Computer Networking a Top to Down Approach (GE) [Internet]. [cited 2024 Aug 7]. Available from: https://www.pearson.com/content/one-dot-com/one-dot-com/se/en/Nordics-Higher-Education/subject-catalogue/computer-science/ross-computer-networking-a-top-to-down-approach-ge.html

63. Peterson, L. L., & Davie, B. S. (2011). Computer Networks: A Systems Approach. Morgan Kaufmann. - Google Search [Internet]. [cited 2024 Aug 7]. Available from: https://www.google.com/search?q=Peterson%2C+L.+L.%2C+%26+Davie%2C+B.+S.+(2011).+Computer+Networks%3A+A+Systems+Approach.+Morgan+Kaufmann.&rlz=1C1ONGR_enUS1109US1109&sourceid=chrome&ie=UTF-8

64. Merrill DR, Bikson M, Jefferys JGR. Electrical stimulation of excitable tissue: design of efficacious and safe protocols. J Neurosci Methods. 2005 Feb 15;141(2):171–98. doi:10.1016/j.jneumeth.2004.10.020 PubMed PMID: 15661300.

65. Rattay F. The basic mechanism for the electrical stimulation of the nervous system. Neuroscience. 1999 Mar;89(2):335–46. doi:10.1016/s0306-4522(98)00330-3 PubMed PMID: 10077317.

66. Thorpe S, Fize D, Marlot C. Speed of processing in the human visual system. Nature. 1996 Jun;381(6582):520–2. doi:10.1038/381520a0

67. Lamme VA, Roelfsema PR. The distinct modes of vision offered by feedforward and recurrent processing. Trends Neurosci. 2000 Nov;23(11):571–9. doi:10.1016/s0166-2236(00)01657-x PubMed PMID: 11074267.

68. Desmurget M, Grafton S. Forward modeling allows feedback control for fast reaching movements. Trends Cogn Sci. 2000 Nov 1;4(11):423–31. doi:10.1016/s1364-6613(00)01537-0 PubMed PMID: 11058820.

69. Blumenfeld Z, Brontë-Stewart H. High Frequency Deep Brain Stimulation and Neural Rhythms in Parkinson's Disease. Neuropsychol Rev. 2015 Dec 1;25(4):384–97. doi:10.1007/s11065-015-9308-7

70. Beurrier C, Bioulac B, Audin J, Hammond C. High-Frequency Stimulation Produces a Transient Blockade of Voltage-Gated Currents in Subthalamic Neurons. Journal of Neurophysiology. 2001 Apr;85(4):1351–6. doi:10.1152/jn.2001.85.4.1351

71. Khantan M, Lim J, Napoli A, Obeid I, Serruya MD. Virtual white matter: a novel system for cross-dish neural interaction and modulation. J Neural Eng. 2025 Jun 1;22(3):036013. doi:10.1088/1741-2552/add49c

72. Bakkum DJ, Chao ZC, Potter SM. Long-term activity-dependent plasticity of action potential propagation delay and amplitude in cortical networks. PLoS One. 2008 May 7;3(5):e2088. doi:10.1371/journal.pone.0002088 PubMed PMID: 18461127; PubMed Central PMCID: PMC2324202.

73. Wagenaar DA, Pine J, Potter SM. Searching for plasticity in dissociated cortical cultures on multi-electrode arrays. J Negat Results Biomed. 2006 Oct 26;5:16.

doi:10.1186/1477-5751-5-16 PubMed PMID: 17067395; PubMed Central PMCID: PMC1800351.